Journal of Geophysical Research: Earth Surface

RESEARCH ARTICLE
10.1002/2017JF004375

This article is a companion to Faug et al. (2018) https://doi.org/10.1002/2018JF004665.

Key Points:
- Snow avalanches exhibit three different stopping mechanisms, and these are primarily controlled by snow temperature
- GEODAR data are used to identify seven flow regimes which are tracked in time and space
- Many avalanches contain multiple flow regimes, and transitions between these regimes are common

Correspondence to:
A. Köhler,
koehler@slf.ch

Citation:
Köhler, A., McElwaine, J. N., & Sovilla, B. (2018). GEODAR Data and the Flow Regimes of Snow Avalanches. *Journal of Geophysical Research: Earth Surface*, *123*, 1272–1294. https://doi.org/10.1002/2017JF004375

Received 24 MAY 2017
Accepted 31 OCT 2017
Accepted article online 25 MAR 2018
Published online 14 JUN 2018

GEODAR Data and the Flow Regimes of Snow Avalanches

A. Köhler[1,2], J. N. McElwaine[2], and B. Sovilla[1]

[1]WSL Institute for Snow and Avalanche Research SLF, Davos, Switzerland, [2]Department of Earth Sciences, Durham University, Durham, UK

Abstract GEOphysical flow dynamics using pulsed Doppler radAR (GEODAR), a custom radar system, images avalanches over the entire slope with high spatial and temporal resolution at the experimental test site Vallée de la Sionne in Switzerland. Between winter seasons 2009/2010 and 2014/2015, data have been acquired from 77 avalanches. These data sets describe a wide variety of avalanches, which we classify in terms of seven flow regimes and combinations thereof. These flow regimes expand on previous classifications, with four identifiable dense flow regimes (where interaction between granules and with the flow bed dominates dynamics) and two different dilute flow regimes (where interaction between snow particles and the air becomes dominant). There is a further regime identified where snow balls simply roll down the mountain. A cold dense regime and a warm shear regime behave like noncohesive granular flows with velocity shear throughout the flow. A sliding slab regime and a warm plug regime occur when cohesion dominates and causes the flow units to act as solid-like objects sliding on a thin shear zone. An intermittent regime connects the cold dense regime with the suspension regime and is characterized by highly fluctuating density and surging activity. GEODAR enables localization of these flow regimes and transitions between them in time and space. We discuss flow regime transitions in terms of snow properties, topography, speed, and size of the avalanches. This paper also serves as a reference for the data set which is made publicly available and should prove to be an invaluable resource for the development of physically based avalanche models.

1. Introduction

Snow avalanches are a major natural hazard in mountainous regions both for people and infrastructure. Large and catastrophic avalanches can reach inhabited areas, and their danger potential is managed with land use planning like hazard maps, temporary measures like road closures, or permanent structures like dams. To successfully design and apply these measures, a quantitative model of the avalanche flow dynamics is essential for prediction of potential runout, impact forces on structures, and the flow around dams.

It has long been known that avalanches can exhibit very different flow behavior (Figure 1), which has led to multiple avalanche classification schemes, for example, Gauer et al. (2008) and De Quervain et al. (1973). In the early stages of avalanche dynamics research, airborne and dense avalanches were differentiated (Voellmy, 1955). The movement of airborne avalanches is controlled by the interaction of particles with air as the flow density is usually low and particles are not in close contact to each other (Hopfinger, 1983). Dense avalanches were further divided into dry and wet avalanches, and the international avalanche classification scheme (UNESCO, 1981) emphasizes the influence of liquid water content. Dry dense avalanches act approximately as noncohesive granular flows, whereas in wet avalanches the cohesion plays an important role and generally causes the mobility to decrease, leading to shorter runouts (Issler, 2003).

Here we emphasize the importance of the snow temperature by classifying regions of avalanches as cold or warm. Indeed, Steinkogler, Gaume et al. (2015) showed recently with small-scale granulation experiments in a rotating drum that there is a sharp transition at around −1°C. Below this temperature individual snow grains keep their identity, but above it the grains rapidly agglomerate into large rounded clumps. This sharp increase in cohesion and therefore in the average particle size by up to 2 orders of magnitude is very important for the dynamic behavior of avalanches (Steinkogler et al., 2014). Naaim et al. (2013) draws a similar conclusion by analyzing many large avalanches in combination with snow cover modeling, finding a temperature dependence of the effective friction.

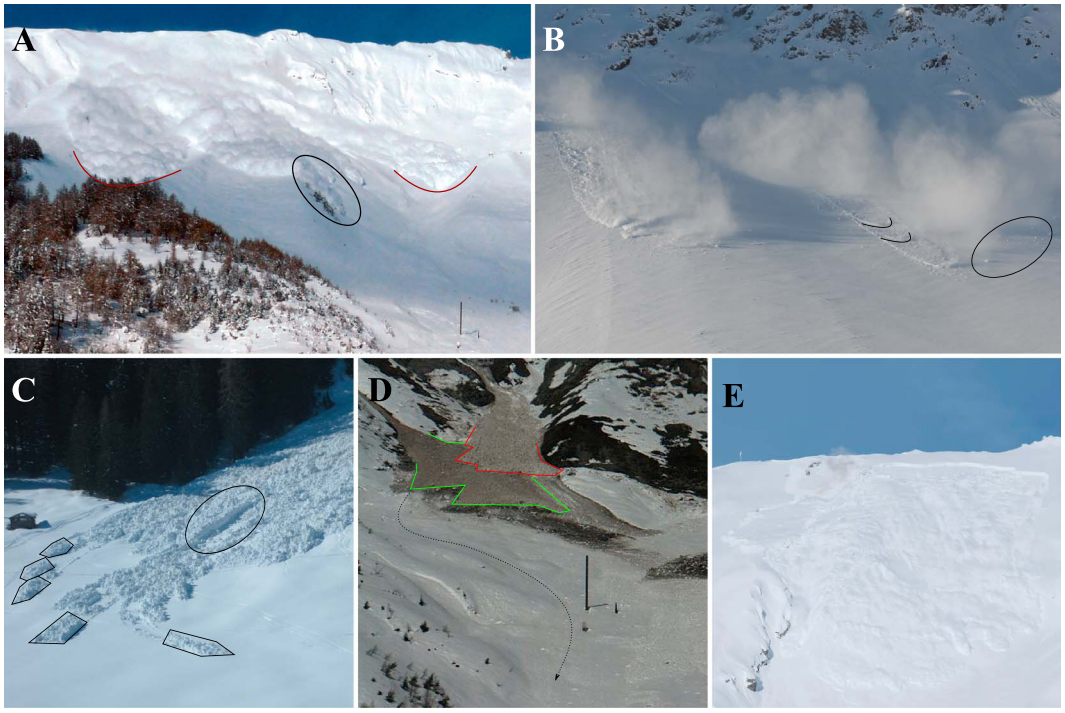

Figure 1. Variety of snow avalanches. (a) Large powder snow avalanche with separate fronts (Vallée de la Sionne [VdlS], #15-0016, Figure 3f). (b) Cold dense avalanche with roll waves and fragments rolling independently (Flüela Pass, Switzerland, 2011; Steinkogler, Sovilla, & Lehning, 2015). (c) Warm plug avalanche with levees and large flow units (Davos, Switzerland, 2015). (d) Two fronts of warm shear avalanche with single granules passing the pylon (VdlS, #12-3060, Figure 7). (e) Fracturing cold slab and the formation of a suspension cloud (VdlS, #15-0020).

The study of the deposits from large avalanches shows that they are often of *mixed* type (Issler, 2003). *Mixed* avalanches are defined as avalanches containing a dense flowing part and a more dilute region (light flow in Schaerer & Salway, 1980, saltation layer in Issler, 1998) under a turbulent suspension or powder cloud. Deposits of avalanches also reveal that the dilute regions usually travel much farther than the denser parts, which supports the theory that mixed avalanches are not only made of layers which feed each other but that these regions can also separate from each other (Gauer et al., 2008). Sovilla et al. (2015) enhanced the understanding by including a comprehensive set of dynamic data (flow height, pressure, density, and velocity) into the typical structure of powder snow avalanches (PSA) (Turnbull & Bartelt, 2003), and characterized the above mentioned regions as dense core, intermittent frontal region and dilute suspension region. The dense core can be further divided into the main body and the tail, and the dilute region into an energetic turbulent suspension, which is fed by the intermittent frontal region, and a decaying powder cloud, where the density and turbulent intensity are decreasing.

In this paper, we use the radar system GEODAR (GEOphysical flow dynamics using pulsed Doppler radAR) (Keylock et al., 2014) to investigate the denser flow processes that are optically obscured under the powder cloud. The radar gives reflectivity data in high spatial (0.75 m) and temporal (111 Hz) resolution. A moving target identification (MTI) processing is applied to the data to remove the nonmoving background clutter. We call the characteristic patterns in MTI images caused by flow structures and by the interaction of the flow with the terrain *MTI signatures*. These can advect with the flow, that is, streaks and lines, or can be induced by local topography, that is, light and dark spots.

We are able to differentiate between starting, flowing, and stopping signatures. The appearance of typical combinations of signatures is connected to the form of movement. Based on that, we characterize the dynamical processes which control the mobility of snow avalanches into different flow regimes and discuss their development in time and space.

The aim of this paper is to improve and extend previous classifications of avalanche flow regimes by using GEODAR data and other measurements and to provide a classification that is based on the physical processes

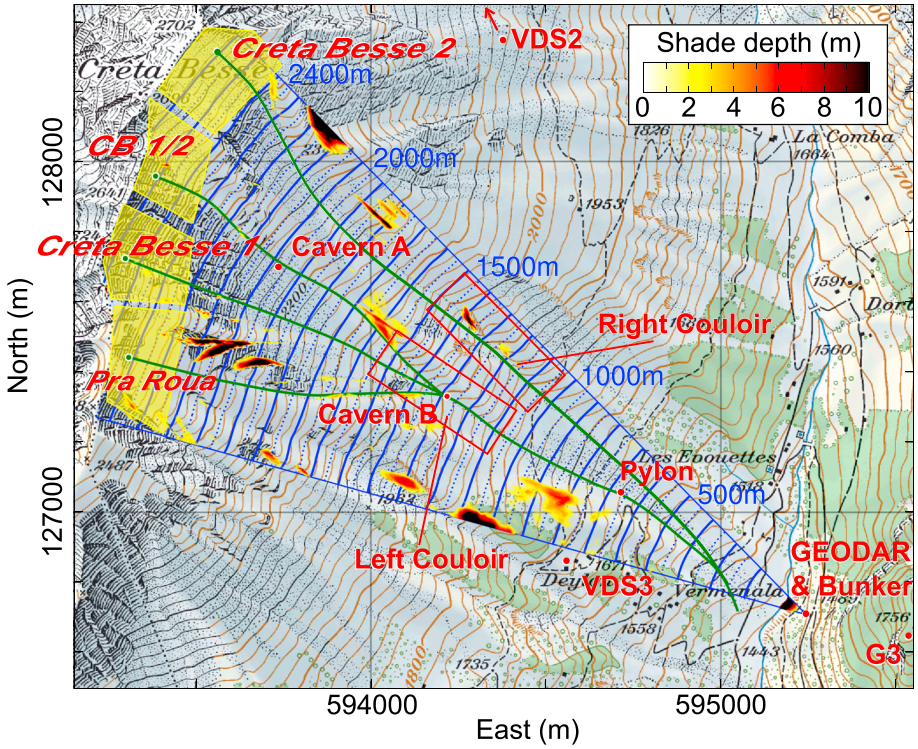

Figure 2. Overview of the Vallée de la Sionne (VdlS) test site. Blue contour lines cover the area observed by GEODAR and indicate the radar range. Areas not visible to GEODAR are colored with the yellow–black color map giving the vertical shadow depth. Red points mark the locations of the pylon, the caverns, the meteo stations, and the bunker hosting the GEODAR system. The four typical release areas are outlined in yellow, and green dots mark the representative coordinate for PRA, CB1, CB1/2, and CB2 release locations giving the typical thalweg as green line. The original map is obtained from the Swiss Geoportal (2015) in Swiss coordinate system CH1903 (SRID 21781). Figure reproduced from Köhler et al. (2016).

that are dominant in different regions. In this paper we define a *region* of an avalanche as a connected volume in space in which the same physical processes are dominant. Groups of physical processes in one region are then defined as *flow regimes*.

The structure of this paper is as follows. In section 2 we explain the different measurement systems and procedures used to generate the raw data and we provide a summary of all the observed avalanches and what data are available. In section 3 we present the avalanche data in detail. We describe typical MTI starting and flowing signatures and identify three different stopping signatures. We connect these with snow cover properties, flow height, and flow velocities. These results lead in section 4 to the definition of seven flow regimes, and in section 5 we give four full-scale avalanche examples to show the occurrence of multiple flow regimes within each event. Transitions between flow regimes are discussed in section 6. Section 7 gives a brief conclusion of the paper. Appendix A lists all acronyms used in the text. Appendix B gives the details of the GEODAR data repository, where documentation of the different versions of GEODAR and more detailed information on radar data processing can be found.

2. Methods and Data

2.1. Vallée de la Sionne Avalanche Test Site

The Vallée de la Sionne (VdlS) avalanche test site is situated in western Switzerland, in Canton Valais (Ammann, 1999). The avalanche path faces southeast and extends between the mountains peaks of Pra Roua and Crêta Besse (Figure 2). The release area is approximately 1,500 m wide, and the total vertical drop is 1,200 m. In the lower section, the path is channeled into two prominent couloirs. Only the left couloir is instrumented, therefore, avalanches releasing from Pra Roua (PRA) toward Crêta Besse (CB1 and CB1/2) provide the widest variety of data, whereas avalanches flowing down Crêta Besse (CB2) are observed only by GEODAR.

The GEODAR system and two cameras are situated 40 m up the counter slope in a concrete bunker facing the avalanche path. In the avalanche runout, a 20-m-high steel pylon is instrumented with sensors at various heights which measure velocity, flow heights, impact pressures, temperatures, and densities (Sovilla et al., 2013). Seismic sensors situated in Cavern B and Cavern A capture the ground motion caused by avalanche activity and trigger the data acquisition. Three frequency-modulated continuous wave (FMCW) radars are installed in the caverns and close to the pylon (Gubler & Hiller, 1984) and are used to extract the flow depth and evaluate the avalanche trajectory. A weather station located close to the avalanche release zone (VDS2) and one at the deposition zone (VDS3) provide information to reconstruct the snow cover conditions along the avalanche path (section 2.4).

2.2. GEODAR

The GEODAR system (GEOphysical flow dynamics using pulsed Doppler radAR) was developed by an international consortium (Brennan et al., 2009) and has been in operation in VdlS since the winter 2010/2011. The GEODAR system hardware and software have undergone continuous improvement. GEODAR I, II, and III built upon the original design (Ash et al., 2010). GEODAR IV was a complete redesign (Ash et al., 2015; Tanha et al., 2017) which unfortunately suffered severely from electronic noise. GEODAR V uses the original hardware but with a different antenna system. Data presented in this paper have been obtained using the first three systems, and each of them is described in detail in the documentation of the data repository (Appendix B).

The radar parameters define the resolution in space and time: the chirp bandwidth of 200 MHz, chirp length 4 ms, and sampling frequency 2 MHz give a range resolution of 0.75 m, a repetition rate of 111 Hz, and a maximum range of 3 km (GEODAR III). The base band frequency is 5.3 GHz, and the corresponding wave length of around 57 mm is roughly the minimal object size providing reflection. Therefore, GEODAR only sees the denser flow structures below the dilute powder cloud (Köhler et al., 2016). A key feature of GEODAR is that it records the full chirp signal as a raw time domain signal. After the data have been acquired the signal can be analyzed in various ways so that improved algorithm design can increase the utility of previously captured data. An important step in the processing chain is the application of a MTI filter. Such filtering is used to suppress the static background signal and enhance different details of the moving avalanche. Here we use a finite impulse response filter with a normalized cutoff frequency of 0.12 and normalize the output for each channel at each range before averaging across all antenna. The signal processing details are described in the data repository documentation (Appendix A).

Typically, the MTI data are displayed in range-time plots, where the radar is at range 0 m, and the MTI intensities are color coded (e.g., Figure 3). The MTI intensities in decibels are related to the reflective area, called the radar cross section. Zero intensity corresponds to the background signal. Positive values quantify the reflection properties of the flow surface and dielectric changes throughout the flow height (Köhler et al., 2016). The avalanche front gives normally the strongest signal, and it appears as a strong step change in the range-time diagram. Many internal avalanche details appear behind the front. Since these internal details are often very faint features, manual extraction and interpretation are necessary. This introduces a certain subjectivity in the results. The error is rather small for the extraction of the front and the back edge or for highly visible internal surges. But the recognition of certain MTI signatures relies to a certain extent on expertise. The detailed description of MTI signatures in section 3.1 provides a classification to make such analyses more consistent between different users. We define *MTI flowing signatures* as those within the flow path and *MTI stopping signatures* as those near where the avalanche stops.

2.3. Release Location, Avalanche Trajectory, and Front Velocity

The release location for each avalanche event was estimated by using four different data sources, namely, pictures, FMCW radars, seismic sensors, and the GEODAR. Pictures of the slope were taken every half an hour. If the full avalanche is visible in the images, we applied a georeferencing scheme to get the full outline and defined the release location as the point of highest elevation (Köhler et al., 2016). For avalanches that occurred during snowfall or periods of cloudy weather (typically PSA), the release location could not be determined from pictures alone. In this case, the FMCW radars and seismic instruments in Cavern B and Cavern A indicate whether the flow went over them and thus determine the favored couloir followed by the avalanche and the most probable release location. Further, the GEODAR image includes characteristic shadow spots which correspond to specific shaded areas in the terrain (Figure 2) and can be used as a terrain orientation.

Knowledge of the avalanche trajectory is crucial to obtain the ground-parallel velocity, since the radar beam hits the terrain surface at a particular line-of-sight angle. We define the 1-D avalanche thalweg as the line

of steepest descent starting from the release location. The procedure to project the range and time data from the front along this thalweg, that is to gain the trajectory s and the ground-parallel front velocity $\dot{s}$, is described in detail in Köhler et al. (2016). Throughout the paper distances are referring to range from the bunker rather than arc length, since the start of an avalanche is often missed due to a delayed trigger.

Even if the release location is not known precisely, the line of steepest descent from a certain region converges quickly to a common thalweg. So for the GEODAR data it is sufficient to know roughly the release region to estimate the ground-parallel velocity in the lower part of the path. In this case, we define the release coordinates (north, east, and altitude in meters) manually for each region in the Swiss coordinate system CH1903 (SRID 21781): PRA [127425, 593311, 2491], CB1 [127663, 593265, 2582], CB1/2 [127930, 593378, 2586], and CB2 [128331, 593540, 2656] (Figure 2).

2.4. Snow Properties

Snow cover properties have a large influence on the avalanche dynamics (Steinkogler et al., 2014). In particular, the snow temperature and the liquid water content are crucial properties which cause different rheological behavior of the flowing snow Naaim et al., 2013; Steinkogler, Gaume et al., 2015).

Unfortunately, very few manual snow profiles are available for the avalanches in our data archive since most of them occurred naturally and the path was rarely accessible immediately after the events. To overcome this problem, we used the numerical model SNOWPACK (Lehning et al., 2002) to reconstruct the snow properties for each avalanche event. The data from two automatic weather stations were used as the input for the simulations. The weather station VDS2 (2,390 m above sea level [a.s.l.]) was used as a proxy for the snow conditions in the release areas, and the weather station VDS3, close to the pylon at 1,680 m a.s.l., was used to reconstruct the snow cover in the deposition area (Figure 2).

The calculated snow properties must be taken with care. In particular, the modeled snow cover will be different from the actual conditions in the flow path since former avalanche activity and entrainment/deposition can alter the old snow cover significantly. However, the SNOWPACK model accounts for energy fluxes within the snow cover through the ground and the atmospheric boundary. The meteo data parameterizing the atmospheric boundary are more important for simulations of new snow precipitation and its metamorphism rather than influences from the old snow cover underneath. Additional uncertainty arise as the simulations were performed on meteo data from flat-field measurements, and incoming global radiation is expected to be different compared to the east facing slopes of Vallée de la Sionne. This results in situations with typical spring conditions, for example, diurnal melt-freeze cycles, in a delayed warming in the simulation compared to expected warming in the avalanche path.

As a first approximation, we define the uppermost 0.5 m of the snowpack to be representative for the snow properties of the flowing avalanche. Snow properties are averaged over this depth, and the simulated snow temperature, liquid water content (Wever et al., 2014), and new snow sum are summarized for each avalanche in Table 1 for the lower ($_b$) and upper ($_t$) weather stations. We have manually chosen the relevant time window up to 6 days before each avalanche to estimate the sum of new snow precipitation.

2.5. Flow Heights

Avalanche flow heights for the cold avalanches in our data archive are derived from FMCW measurements performed in Cavern B (Gubler & Hiller, 1984). FMCW radars operate like ground penetrating radar but point up through the flowing snow rather than downward to the ground. Due to large attenuation of the electromagnetic signal by liquid water content, the radars have limited usefulness in wet snow conditions or if large snow deposits cover the radar. For nearly all warm flow avalanches no flow height information from FMCW can be obtained.

The interpretation of the FMCW radar signal is not straightforward since the signal is influenced by multiple reflections of layers in the snowpack (Schmid et al., 2014), and the depth accuracy is dependent on the unknown density of the snow pack as well as the flowing snow. Nevertheless, the FMCW radar gives a detailed but qualitative picture of the flowing avalanche including entrainment, deposition, flow height changes, wave heights, and flow structure (Sovilla et al., 2006). Flow heights of surges and waves were manually extracted and connected to the surge flowing signatures in the GEODAR data (Köhler et al., 2016).

2.6. Avalanche Cadastre

Since the initial deployment in December 2010 until May 2015, the GEODAR system has measured 77 avalanche events, summarized in Table 1. Each avalanche is identified by the archive number (column SLF-Nr)

Table 1
List of Avalanche Events Recorded With GEODAR System

SLF-Nr	GEODAR time stamp	Release	Altitude (m)	Runout (m)	Stop	Slope (deg)	v_s (m/s)	Img	A	B	C	TS_b (°C)	TS_t (°C)	LWC_b (%)	LWC_t (%)	HN_b (cm)	HN_t (cm)
20113002	2010-12-06-07-46-21	CB2	>2,600	360	A	21	15	1	0	0	0	–	−4.3	–	0.0	–	27
20113003	2010-12-06-18-36-18	PRA	>2,500	490	A	23	16	1	0	1	1	–	−2.3	–	0.0	–	41
20113004	2010-12-07-03-36-43	CB1/2	>2,600	150	–	23	8	1	1	1	1	–	−1.9	–	0.0	–	54
*20123013	2011-12-19-15-16-02	CB1/2	~2,550	1,560	A	30	13	0	–	–	–	–	−11.3	–	0.0	–	125
20123023	2011-12-30-23-55-22	CB1/2	>2,100	670	A	23	15	0	0	1	–	–	−9.1	–	0.0	–	50
20123024	2011-12-31-06-59-34	Unknown	–	1,820	A	–	15	0	–	–	–	–	−7.0	–	0.0	–	56
20123026	2011-12-31-07-44-25	CB1	>2,300	850	A	22	14	0	0	1	–	–	−6.5	–	0.0	–	58
20123028	2011-12-31-09-01-41	Unknown	–	670	A	–	19	0	0	1	–	–	−6.1	–	0.0	–	61
20123029	2012-01-02-21-22-15	PRA	1,906	995	C	26	2	2	–	–	–	–	−4.5	–	0.0	–	13
20123031	2012-01-04-07-21-42	CB1	>2,100	965	C	25	14	0	0	1	0	–	−4.3	–	0.0	–	16
20123032	2012-01-04-07-42-50	CB1/2	>2,600	955	C	25	19	0	1	1	0	–	−4.2	–	0.0	–	16
20123035	2012-01-05-16-45-21	CB1/2	>2,650	150	A	18	28	1	1	1	1	–	−5.1	–	0.0	–	26
20123040	2012-01-10-00-03-06	PRA	2,264	675	B	23	16	2	–	–	–	–	−7.8	–	0.0	–	0
20123041	2012-01-12-17-19-07	CB1/2	2,500	1,255	B	30	18	2	–	–	–	–	−6.1	–	0.0	–	0
20123042	2012-01-13-02-42-41	CB1/2	2,014	1,000	C	26	2	2	–	–	–	–	−7.4	–	0.0	–	0
20123048	2012-02-03-16-25-32	CB1	2,051	850	B	22	16	2	–	–	–	–	−8.8	–	0.0	–	0
20123051	2012-02-24-12-24-47	CB1/2	2,586	1,395	–	38	6	2	–	–	–	–	−7.5	–	0.0	–	0
20123053	2012-02-29-16-48-02	CB1	2,394	940	C/B	24	15	2	–	–	–	–	−4.0	–	0.6	–	0
20123055	2012-03-01-14-44-36	PRA	2,540	930	C	24	9	2	0	0	–	–	−3.0	–	0.8	–	0
20123060	2012-03-15-10-56-28	PRA	2,458	950	B	25	17	2	0	0	–	–	−1.9	–	0.1	–	0
20133003	2012-12-04-04-46-05	CB1	>2,450	545	A	23	25	1	0	1	1	−0.8	−4.4	0.0	0.0	50	59
20133005	2012-12-06-01-54-50	CB1	>2,200	890	A	23	16	0	0	1	–	−5.5	−9.8	0.0	0.0	87	94
20133006	2012-12-07-14-00-39	Unknown	–	1,625	A	–	12	0	–	–	–	−5.5	−10.1	0.0	0.0	79	102
20133007	2012-12-10-08-12-49	CB1/2	>2,050	825	A	22	14	0	0	1	–	−4.4	−9.1	0.0	0.0	34	35
20133018	2013-02-01-16-52-45	CB1/2	>2,500	880	C	22	10	1	1	1	–	0.0	−2.2	1.7	0.0	15	35
20133019	2013-02-01-17-14-50	CB1/2	>2,450	200	C	19	1	1	1	1	1	0.0	−2.2	1.7	0.0	15	35
20133020	2013-02-01-20-18-46	CB2	>2,600	155	C	18	2	1	–	1	–	0.0	−2.2	1.8	0.0	15	44
20133021	2013-02-02-05-27-31	PRA	>2,450	180	C	18	6	1	0	1	1	−0.0	−2.6	1.9	0.0	15	69
20133022	2013-02-02-15-38-13	CB1	2,069	960	B	25	10	1	–	1	–	−0.3	−5.8	1.6	0.0	25	79
20133023	2013-02-05-21-13-35	CB1	~2,250	1,190	A	30	16	0	0	1	–	−1.4	−6.3	0.2	0.0	44	92
20133024	2013-02-05-23-31-53	CB1/2	~2,600	460	A	22	18	0	1	1	0	−2.5	−8.1	0.0	0.0	52	99
20133025	2013-02-19-13-13-31	CB1/2	2,506	1,775	A	29	8	2	–	–	–	−2.4	−6.5	0.0	0.0	0	0
20133028	2013-03-02-11-46-45	CB1/2	2,029	940	B	24	12	2	–	–	–	−0.8	−5.8	0.1	0.0	0	0
20133030	2013-03-03-11-29-11	CB1/2	2,608	1,940	–	34	10	2	–	–	–	−0.6	−6.1	0.4	0.0	0	0
20133031	2013-03-03-12-23-33	CB1/2	2,602	1,900	–	31	10	2	–	–	–	−0.6	−5.4	0.4	0.0	0	0
20133037	2013-03-18-23-50-57	CB1/2	>2,550	1,720	A	28	18	0	1	–	–	−1.1	−6.0	0.0	0.0	16	45
20133038	2013-03-19-03-24-48	Unknown	–	1,125	A	–	16	0	–	–	–	−1.7	−7.3	0.0	0.0	24	57
20133040	2013-03-19-04-21-42	CB1	>2,100	1,050	A	27	19	0	0	0	–	−1.7	−7.8	0.0	0.0	24	58
20133041	2013-03-22-10-03-29	CB1/2	2,547	1,525	A	30	7	1	1	0	–	−0.0	−3.1	0.6	0.0	38	40
20133043	2013-04-06-18-35-09	CB1/2	2,486	1,725	C	28	2	2	–	–	–	0.0	−1.7	2.6	0.0	0	0
20133044	2013-04-06-19-23-47	CB1/2	2,488	1,010	B	26	20	2	–	–	–	0.0	−1.7	2.6	0.0	0	0
20133046	2013-04-10-15-07-55	PRA	2,350	990	C	26	6	2	–	–	–	0.0	−1.0	2.8	0.1	29	44
20133047	2013-04-12-13-33-47	PRA	2,319	785	C	21	17	2	–	–	–	0.0	−0.5	3.1	0.1	0	37
20133048	2013-04-13-04-06-44	CB1	2,432	775	C/B	21	1	2	–	–	–	−0.1	−1.8	1.8	0.0	10	51
20133049	2013-04-13-12-37-24	CB1	2,300	965	C/B	25	5	2	–	0	–	−0.0	−0.4	3.2	0.2	10	51

Table 1 *(continued)*

SLF-Nr	GEODAR time stamp	Release	Altitude (m)	Runout (m)	Stop	Slope (deg)	v_s (m/s)	Img	A	B	C	TS_b (°C)	TS_t (°C)	LWC_b (%)	LWC_t (%)	HN_b (cm)	HN_t (cm)
20133050	2013-04-13-14-19-46	CB1/2	2,380	995	B/C	26	11	2	–	0	–	0.0	−0.4	3.2	0.3	10	51
20133051	2013-04-13-23-59-42	CB1	2,215	975	C/B	25	4	2	–	0	–	−0.2	−0.9	1.8	0.1	10	51
20133052	2013-04-14-11-25-56	CB1/2	2,501	1,795	B/C	29	18	2	–	0	–	0.0	−0.6	3.5	0.2	0	14
20133053	2013-04-14-22-49-51	CB1/2	2,415	960	C/B	25	4	2	–	0	–	−0.0	−0.3	2.1	1.3	0	0
20140011	2014-02-13-17-37-30	CB1/2	>2,450	1,150	A	29	13	0	–	1	–	−2.2	−3.8	0.0	0.0	27	28
20140012	2014-02-13-19-21-32	CB1/2	>2,500	160	A	18	30	0	1	1	1	−2.2	−4.3	0.0	0.0	32	38
20140013	2014-02-20-11-15-05	CB1/2	2,596	1,890	A	32	9	2	–	–	–	−1.2	−3.2	0.0	0.0	18	20
20140014	2014-02-21-14-53-19	CB1	2,210	770	C/B	21	1	2	–	–	–	−0.8	−1.8	0.0	0.0	0	0
20140016	2014-03-11-11-54-57	CB1	2,042	1,000	C	26	6	2	–	–	–	−0.5	−2.0	0.2	0.1	0	0
20140017	2014-03-12-13-09-43	PRA	~2,250	1,160	B/C	34	9	0	0	0	–	−0.4	−1.8	0.4	0.2	0	0
20140019	2014-03-13-14-30-06	CB1/2	2,483	1,610	C	30	6	2	–	–	–	−0.0	−1.1	1.1	0.7	0	0
20150003	2014-12-27-20-18-49	CB1	~2,550	600	A	24	22	0	0	1	1	−6.4	−9.2	0.0	0.0	57	73
20150004	2014-12-27-22-38-15	Unknown	–	1,105	A	–	19	0	0	0	–	−6.7	−9.7	0.0	0.0	61	73
20150009	2015-01-29-05-18-08	CB2	~2,550	710	A	18	18	0	0	1	–	−1.3	−5.3	0.0	0.0	21	26
20150011	2015-01-29-06-22-02	CB1/2	>2,450	860	B	22	24	0	1	1	–	−1.3	−5.4	0.0	0.0	22	31
20150013	2015-01-30-02-12-22	CB2	~2,650	100	A	18	29	0	0	1	1	−3.6	−7.3	0.0	0.0	42	78
20150015	2015-01-30-20-58-55	CB1/2	>2,450	1,085	A	28	12	0	1	1	–	−5.2	−10.5	0.0	0.0	51	93
*20150016	2015-02-03-10-20-16	PRA	2,510	100	–	18	34	2	0	1	1	−4.2	−10.0	0.0	0.0	50	97
*20150017	2015-02-03-11-45-30	CB1	2,574	110	–	18	43	2	0	1	1	−2.0	−8.7	0.0	0.0	50	97
*20150019	2015-02-03-11-54-44	CB1/2	2,606	870	A	22	8	2	1	1	–	−2.0	−8.7	0.0	0.0	50	97
*20150020	2015-02-03-12-04-39	CB2	2,649	150	A	18	17	2	0	1	1	−2.0	−8.7	0.0	0.0	50	97
*20150022	2015-02-03-12-14-47	CB1/2	2,607	970	A	25	16	2	–	–	–	−2.0	−8.7	0.0	0.0	50	97
20150028	2015-03-11-12-16-07	CB1/2	2,471	1,835	–	30	5	2	–	–	–	0.0	−1.4	0.0	0.1	–	0
20150035	2015-04-03-11-42-26	CB1	>2,400	945	C/B	25	1	0	0	0	–	–	−0.1	–	0.1	–	78
20150037	2015-04-03-12-39-00	CB1/2	>2,450	1,220	B	30	3	0	0	0	–	–	−0.1	–	0.2	–	78
20150038	2015-04-03-13-04-39	Unknown	–	1,985	–	–	5	0	0	–	–	–	−0.1	–	0.2	–	78
20150040	2015-04-08-22-35-13	CB1/2	2,497	765	C	21	1	2	–	–	–	–	−1.1	–	0.1	–	23
20150043	2015-04-09-17-21-45	CB1	2,212	955	B	25	4	2	–	–	–	–	−0.2	–	1.4	–	23
20150044	2015-04-10-16-11-33	CB1/2	~2,400	1,170	C	29	10	0	0	0	–	–	−0.1	–	1.8	–	0
20150046	2015-04-11-10-05-55	CB1/2	2,481	1,890	–	31	5	2	–	–	–	–	0.0	–	1.7	–	0
20150047	2015-04-11-14-37-05	PRA	2,215	1,100	C	28	10	2	–	–	–	–	0.0	–	1.7	–	0
20150048	2015-04-12-00-08-39	CB1	2,376	1,315	B	34	8	2	–	–	–	–	−0.2	–	1.5	–	0

Note. For a detailed description see section 2.6. The first 8 columns summarize metadata including release area, runout, stopping signature, and velocity vs. Columns 9 to 12 contain the availability of additional data from cameras, Caverns A and B, and the pylon (C). The last 6 columns give meteorological and nivological conditions.

which is the hydrological season followed by a four-digit running number. The GEODAR data are identified by the trigger time stamp (column GEODAR time stamp) in the date format year-month-day-hour-minute-second. Most of the avalanches were naturally released, and only few were artificially released during an experiment. Artificially released avalanches are marked with an asterisk in the column SLF-Nr in Table 1.

The columns 3 to 8 of the Table 1 contains metadata and information directly derived from the GEODAR measurements. The release area and altitude are derived as described in section 2.3, and the runout length is defined as the smallest radar range reached by the avalanche (Pérez-Guillén et al., 2015). The column "stop" characterizes the stopping signatures visually identified from the GEODAR plots: (A) starving, (B) backward propagating shock, and (C) abrupt stopping (section 3.2). For some events a combination of two stopping signatures exists. In such case, we have indicated this by mentioning the main and a subsignature. For avalanches which stopped above a range of 1,800 m (sluff avalanche size) or stopped in the valley floor (very large), no stopping signature could be inferred (–). We also average the slope angle over the last 100 m (range)

of the trajectory before the avalanche stops, and give the velocity v_s at 100 m in range before the stopping point. This is an arbitrary distance which we chose since we have these data for a large number of avalanches and it gives a robust measure of the avalanche speed and the following deceleration.

Pictures prior to and after the event (column Img) are number coded regarding their information content: (0) no images, (1) deposit visible as lower path outline, and (2) full outline. Availability of FMCW data in Cavern A and B (column A and B) is coded with the following criteria: (1) avalanche signal, (0) no avalanche signal, and (−) missing signal due to wet snow interference. Column C indicates the availability of pylon measurements.

The columns 13 to 18 of Table 1 contains information on the snow cover derived from snowpack simulations as described in section 2.4. The columns TS_b, TS_t, LWC_b, and LWC_b are the mean snow cover temperatures and the liquid water content at the bottom $_b$ (VDS3) and top $_t$ (VDS2) weather stations and refer to the average of the uppermost 50 cm of the snow cover. The columns HN_b and HN_t are the sums of new snow precipitation in up to 6 days prior to the avalanches at the bottom and top stations, respectively.

3. Results

Snow avalanches are geophysical flows with diverse flow behaviors of which some of them are shown in the pictures in Figure 1, and with different composition of *flow units* from fine grained to rounded granules to large clusters as shown by Ancey (2007). Note, we are using *unit* in its geological sense. *Units* are the basic units of geologic mapping and refer to regions with similar properties. The GEODAR radar enables to observe this wide diversity even in weather condition of low visibility and — more important — through an opaque powder cloud. Differences can be observed in the radar signatures of the internal flow structures and in particular in the stopping signatures, which we categorized into three types. We also present data on flow velocities, snow properties, and flow height where this is available.

For naturally released avalanches the GEODAR system is triggered seismically from geophones in Caverns A and B, so, generally we miss the initial release and early stages of the flow. For artificially released avalanches this problem does not arise, and in addition sometimes a sequence of multiple avalanche released only a few minutes apart could be captured.

3.1. MTI Flowing Signatures

Figure 3 is a collection of GEODAR flowing signatures which frequently occur in our data. The top row shows streak signatures which move with the flow, and the bottom row shows internal signatures which are fixed relative to the topography. We discuss them in more detail in section 4 when connecting them with flow regimes.

The GEODAR images show most clearly the front (Figure 3a) and the tail of an avalanche. Inside the avalanche, where the flow is steady, the signature is homogeneously colored (Figure 3a). If, instead, internal structures in the flow exist, they become visible because they are in general a sequence of darker and light MTI intensities.

The most obvious flowing signatures in the MTI are dark streaks (Vriend et al., 2013), whose steepness give the flow velocity toward the radar. Köhler et al. (2016) connected these streaks to internal surges, which are denser and give stronger reflections than the surrounding flow. These surges can have long trajectories and appear throughout the full avalanche (Figure 3b), or they can have short trajectories and exist only in the proximity of the avalanche front (Figure 3c).

Figure 3b shows an example of long trajectory surges. These surges can be generated when the topography splits the avalanche into several arms, in which case we call them separate fronts (Figure 1a). Or they can originate from secondary slab releases and move along the same thalweg in which case we call them major surges (Köhler et al., 2016). In both cases, they can be regarded as individual avalanches with independent flow dynamics and flow regimes (Köhler et al., 2016).

Figure 3c shows an example of short trajectory surges. These minor surges only occur in fully developed PSAs. As long as they are behind the front, they can have velocities larger than the front velocity, and thus, they have a large influence on the front dynamics and avalanche mobility due to overrunning (Köhler et al., 2016).

Figure 3d shows an example of streaks often present in very slow avalanches. These streaks are running parallel to the front and are probably the result of flow units which change their structure only little during motion. Figure 1c shows an example picture of such solid-like flow units, which did not interact with each other.

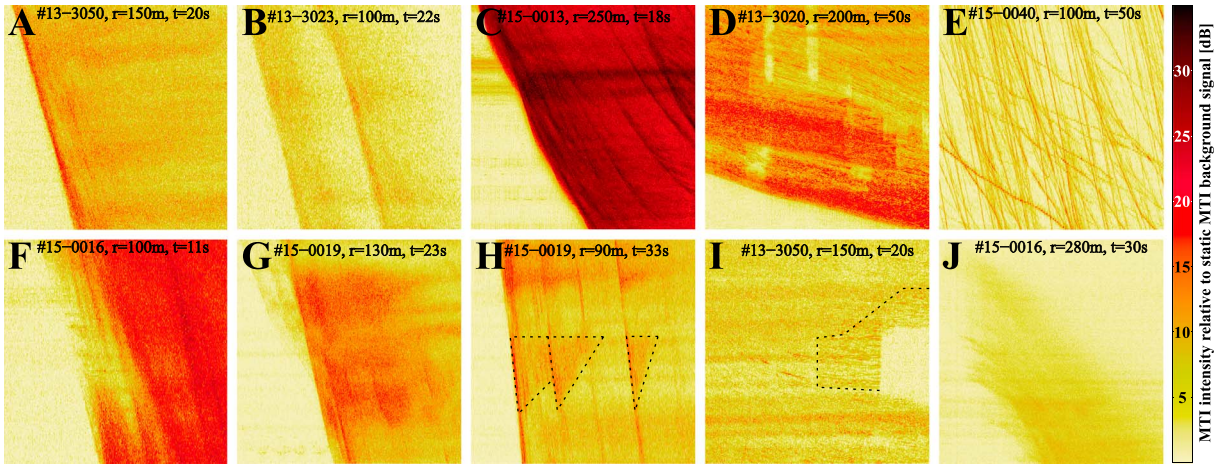

Figure 3. Common GEODAR flowing signatures of snow avalanches. (a–e) Streak signatures indicating structures flowing with the avalanche. (f–j) Signatures of flow structures that are connected to a location in the avalanche path. Avalanche number and scale in range *r* (*y* axis) and time *t* (*x* axis) are included in each panel. The color scale of logarithmic moving target identification intensity is the same in all panels.

Often completely blank spots are visible together with this parallel streak signature (Figure 3d). These blank spots can have zero intensity even when the surrounding signal can be very strong. The location of these blank spots depends on the frequency response of the MTI filter. They may occur when the flow surface is smooth so that there is no change in reflected amplitude from one chirp to another or in cases where the variations are narrow band are filtered out by the MTI filter.

Beside streaks which are located inside the avalanche, we can identify single line features often starting from the main deposit or running in front of the avalanche as shown in Figure 3e. Comparison with videos and photos of the debris reveal that these are traces of single snowballs or snow wheels (Figure 1b). These have been observed to roll down the slope for as far as 1 km (Figure 7 or in 1d).

Some types of flowing signatures always occur in the same place on the slope and do not advect with the avalanche flow, so that it is strongly suggestive that they are triggered by certain topographic features. They can be areas of greater or lesser variation in reflected signal corresponding to darker or lighter signatures in the MTI plots. Figure 3f shows an example of a light spot typically observed in avalanches from the PRA release area. The location of the spot corresponds to a shaded area, which is not reached by the GEODAR beam because of topographic obstructions (Figure 2). Figure 1a shows the corresponding picture of this avalanche: The suspension cloud overtops the small gully (black circle), while the denser parts are shaded from the radar. These spots can be used as a reference to trace the avalanche trajectory and to estimate an upper limit of the flow height of denser material below the suspension cloud.

Figure 3g shows an example of a darker region. This one is located at 1,350 to 1,450 m and corresponds to the steep entrance of the couloir. The dark spot indicates an increase in radar cross section (Salm & Gubler, 1985). In steep terrain, the avalanche head may become more turbulent or fluidize and may exhibit a larger area causing reflections of the signal.

Figure 3h shows that avalanches may contain structures which leave a triangular outline in the MTI plots. Here the avalanche consists of four surges of which three trigger a triangular signature beginning at the same range. While the upper boundary is connected to a certain location, the lower boundary moves upward with time. These are presumably standing shocks or jets triggered by topography. This particular avalanche has been described with flow height and velocity data in Köhler et al. (2016).

Figure 3i shows that the flowing signature can change locally and may indicate an abrupt change of the flow properties. This panel shows further that almost any radar image contains horizontal bands (e.g., see Figures 7 to 10). When they exist through the full recording length or are outside the avalanche area, they belong to noise from electronic or environmental sources like waving trees in the wind (Figure 10). But such horizontal bands can also appear inside avalanches and may result from interaction with topography.

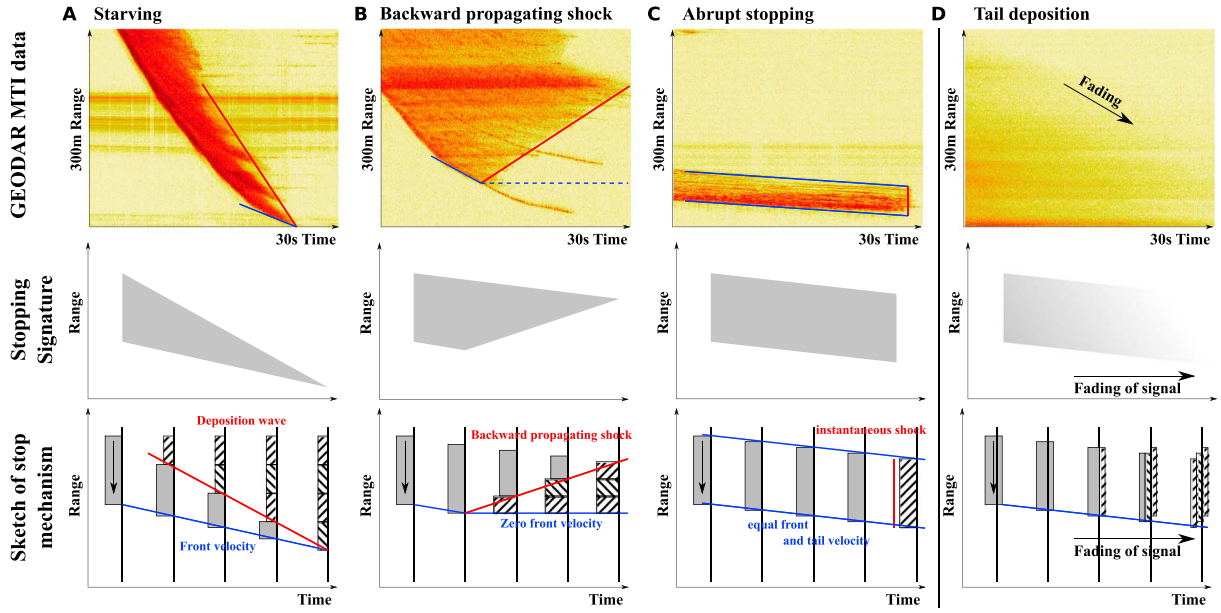

Figure 4. (top row) Four stopping signatures of avalanches measured in Vallée de la Sionne: (a) starving (#11-3002), (b) backward propagating shock (#12-3048), (c) abrupt stopping (#14-0014), and (d) tail deposition (#15-0009). (middle row) The characteristic stopping signature is shown below as a synthetic moving target identification (MTI). (bottom row) Sketch of the corresponding stopping mechanism. Only moving parts (gray), but not deposits (striped), will show up in the synthetic MTI. The MTI is in fact the gray area of the sketch.

Finally, for a few avalanches we have captured the release of the snow slab as Figure 1e shows. It is possible to observe the complete slab starting simultaneously and leaving a vertical starting signature in the MTI plot. While in the beginning some streaks may indicate the movement of large snow blocks, with time the signature becomes homogeneous as the blocks fragment to small grains (e.g., Figure 3j). Point release avalanches would give a different MTI starting signature (Figure 9c), but we have little data on this, presumably because we miss the start of the vast majority of avalanches.

3.2. MTI Stopping Signatures

The stopping phase of an avalanche is nearly always recorded by the GEODAR system. By *stopping signature* we mean the pattern which the stopping mechanism of the avalanche traces in the radar images. We identify three distinct stopping signatures in the data sets, with typical examples shown in Figure 4.

We define the corresponding stopping mechanisms as: (A) starving, (B) backward propagating shock, and (C) abrupt stopping. A further tail deposition mechanism (D), often visible at large ranges, has also been included. The stopping signatures (A–C) were manually assigned to each avalanche event and summarized in Table 1 in column "stop". In the following we describe the characteristics of each deposition mechanism.

Starving (Figure 4a). Almost 40% of the avalanches in the database are characterized by a progressive decrease in avalanche flowing length just before deposition. Material is deposited at the avalanche tail, while at the same time, the front continues to flow. The flowing length gradually diminishes, and the front finally starves. Only a small part of the avalanche mass reaches the final runout position. This mechanism is often associated with the presence of surging in the avalanche flow (Köhler et al., 2016). The avalanche deposits are usually smooth and widespread (Issler, 2003), and the deposit heights are generally lower than the flow height (Sovilla et al., 2010).

Backward propagating shock (Figure 4b). Around 20% of the avalanches in the database are characterized by a stop of the avalanche front, followed by a progressive piling up of the incoming material. There is an upslope or backward propagating shock clearly visible on the MTI plots. Often the shock travels with a fairly constant velocity and appears as an upward sloping line in the MTI plots. The shock velocity is a phase and not a group velocity: only the shock wave and no material travels upward (Köhler et al., 2016). Typically, the deposits of these flows are rough and granular, but they have little large scale structure above the size of the snow particles or blocks.

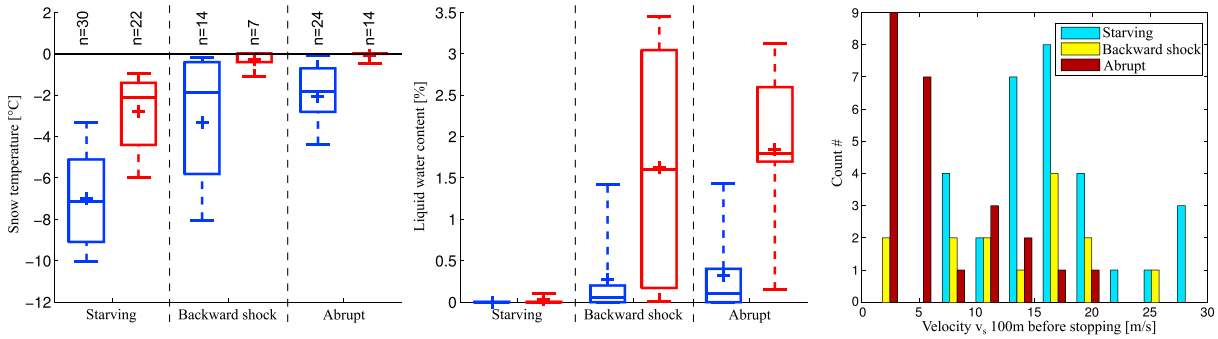

Figure 5. Correlation of stopping mechanisms with snow cover properties and front velocity. Box plots for snow temperature (left) and liquid water content (middle) correspond to quantities averaged over the uppermost 0.5 m of the snowpack. The snow conditions in the release area are represented by the weather station VDS2 (blue), and for the deposit region by the weather station VDS3 (red). The number of data per box are given by *n*, cross gives the mean, line is the median, the box spans the interquartile range, and the whiskers show the 9th to 91st percentiles. (right) Histogram of v_s, the velocity 100 m before the avalanches stop.

Abrupt stopping (Figure 4c). Around 30% of the avalanches in the database are characterized by an abrupt and almost instantaneous stop throughout the complete flow length. This stopping mechanism is characterized by a vertical signature in the MTI plots. The signal is often characterized by streaks which run parallel to the avalanche front and avalanche tail, suggesting that the avalanche velocity is constant over large parts of the flow. Typically, these flows are laterally confined by levees or icy shear planes and the deposits are often rough with steep and sharp boundaries (Issler, 2003). For around 30% of these avalanches, the dominant abrupt stopping mechanism coexists with the backward propagating shock mechanism, for example, Figure 7c and at 1,000 m in Figure 8.

Tail deposition (Figure 4d). Snow deposition can occur not only in the avalanche runout zone but also along the avalanche path when the slope angle is smaller than around 30° (Sovilla et al., 2010). Indeed, at higher altitudes the MTI plots are often characterized by a gradual decrease in MTI intensity toward the tail. Such a signature is consistent with a progressive decrease in flow depth which can be caused by both loss of material at the avalanche base or by the avalanche elongation and consequent retention of material at the avalanche tail (Sovilla et al., 2010).

3.3. Snow Properties and Flow Velocity in the Stopping Phase

In Figure 5, we connect each stopping mechanism with the snow temperature (left) and the liquid water content (middle) and give the distribution of front velocity v_s corresponding to the velocity at 100 m in range before the avalanches stop (right).

The starving deposition mechanism (Figure 4a) is a specific feature of cold avalanches, that is, avalanches with average snow temperature below −1°C. At these temperatures snow has a low ability to sinter and to form granules, and fragmentation is more important than aggregation (Steinkogler, Gaume et al., 2015). The avalanche composition is mostly fine grained material and some fragments of released slabs and entrained snow.

In contrast, the backward propagating shock (Figure 4b) is characteristic for avalanches with average snow temperatures close to 0°, at least in the deposition zone (Figure 5). For the liquid water content our data are inconclusive due to a large variation between 0.2 % and 3% caused by only seven data points in the box plots but greater than for the starving deposition mechanism. For these snow cover characteristics we believe that aggregation of snow crystals exceeds fragmentation and may give rise to the formation of persistent-moist granules (Steinkogler, Gaume et al., 2015). However, this stopping mechanism can also occur in dry granular flows (Gray et al., 2003), if they encounter a sharp reduction in slope angle or increased surface roughness such as preexisting debris, so we also expect this on occasion for cold snow.

For avalanches with an abrupt stopping signature (Figure 4c), the conditions for cohesion leading to the formation of persistent-wet granules (Steinkogler, Gaume et al., 2015) prevail for snow temperatures reaching 0°C and LWC above 1.8%.

The front velocities v_s (Figure 5, right) give a measure of the avalanche deceleration during the last 100 m in relation to each stopping mechanism. Avalanches characterized by a starving stopping mechanism are

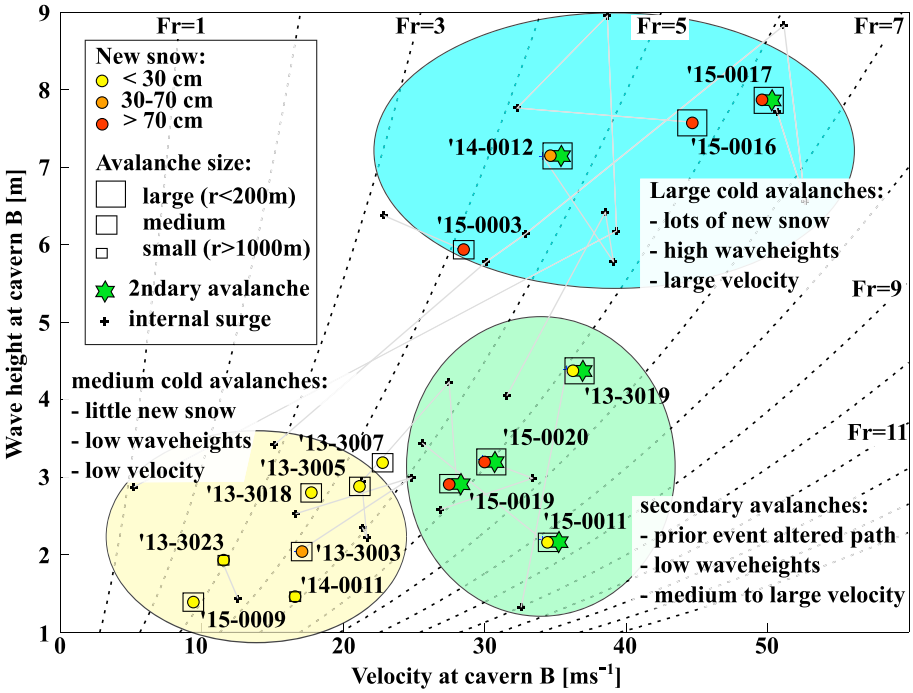

Figure 6. Flow heights of cold avalanches as a function of the velocity at Cavern B. The front is indicated by symbols, which give the amount of new snow (circle), the avalanche size in runout range (square), and whether it was a secondary avalanche (star). Small black crosses belong to internal surges, and gray lines connect the consecutive surges with the front. Froude numbers *Fr* are shown with black dashed lines in the background.

the fastest with up to 30 m/s (blue). Note that the largest avalanches reaching the valley bottom had to be excluded from this analysis since their stopping could not be observed, so that the distribution is biased toward smaller velocities.

In contrast, avalanches characterized by abrupt stopping are the slowest with even large avalanches having velocities of only up to 5 m/s (red). The few higher velocities belong to medium sized avalanches which present a mix between abrupt and backward propagating shock stopping mechanisms and for which the abrupt stopping signature appear shortly before stopping. They are indicated with "C/B" in Table 1 and bias the velocity distribution toward higher values.

The velocities of avalanches characterized by the backward propagating shock mechanism are in between these extremes. Most of them have a flow velocity of around 10 to 20 m/s (yellow).

Given that the avalanches have different sizes and stop at different locations along the path, it is in general complicated to compare the velocities directly and leads to greater error in the velocity distribution. Even with this uncertainty, the velocity data show clearly a trend between the three stopping signatures (Figure 5).

3.4. Flow Height and Velocity of Cold Avalanches

Avalanches characterized by the starving stopping mechanism give a broad distribution of velocities v_s (Figure 5, right), since they can cover a large range of runouts (Table 1). We investigate their flow characteristics in more detail at the location of Cavern B.

We extracted the flow heights of the front and consecutive surges from the FMCW profiling radar and related them to the corresponding flow velocities from the MTI plots at Cavern B (Figure 6). Circles and square symbols indicate the amount of new snow and avalanche size, respectively. A star indicates secondary avalanches which happen after previous avalanche activity and thus find different flow bed conditions in their path. We have identified three different clusters highlighted with blue, yellow, and green circles. Interestingly, we did not record any primary avalanche with flow heights in between the blue and yellow clusters; even so the velocity between both clusters is smooth.

The Froude number is defined as $Fr = \dot{s}/\sqrt{gh\cos\theta}$ and gives a measure of whether the flow is supercritical or subcritical (black dashed lines in Figure 6). All cold avalanches have Froude numbers *Fr* between 3 and 8, and from a hydrodynamic point of view, their flow is supercritical and their motion is most likely turbulent or fluidized (Issler, 2003). There is a little trend to higher *Fr* with avalanche size and amount of new snow precipitation.

The *blue cluster* contains large avalanches which happened after significant snow fall events with precipitation of more than 70 cm new snow. All large avalanches in this cluster reached the valley bottom. The flow heights were between 5 and 8 m, and the velocities were as high as 30 to 55 m/s. Minor surges are found in the blue cluster as well.

The *yellow cluster* contains small- to medium-sized avalanches which starved shortly below Cavern B or at the end of the couloir. Previous snowfall gave mostly not more than 30 cm of new snow. The flow heights were limited to around 3 m, and the velocities did not exceed 25 m/s. Additionally, some second surges appear in the yellow cluster and indicate the dense core and dense tail region of larger avalanches (Sovilla et al., 2015).

The *green cluster* contains secondary avalanches that followed a reasonably large previous event in the same path; for example, #15-0017 and #15-0019 were released shortly after #15-0016. The snow cover was therefore altered, and the avalanches found less fresh snow but only harder deposits to entrain. These avalanches had high velocities between 25 and 40 m/s but relatively low flow heights up to 4 m. The Froude number was highest for these avalanches. Some internal surges appear in the green cluster as well.

4. Avalanche Flow Regimes

The GEODAR plots of avalanches at the Vallée de la Sionne can exhibit a large variety of MTI flowing and stopping signatures as described in section 3. By combining these signatures with the snow cover conditions at the moment of the event, we identify seven different flow regimes. The MTI flowing signatures are not always enough to uniquely classify each regime, but in conjunction with the MTI starting and stopping signature each regime can be unambiguously identified. For example, the warm shear (WSR) and the cold dense regime (CDR) do not differ much in the MTI flowing signature, both are homogeneous and can have similar velocities, but the stopping signature and the snow temperature data separate both regimes. We will not discuss glide snow or slush flow regimes as these have not occurred in our data from Vallée de la Sionne.

In the following we will give a short definition for each of the flow regimes and we will link them to the MTI signatures and snow cover properties. In section 5 we will show that avalanches are made of a combination of different flow regimes, and finally we will discuss in section 6 how transitions between flow regime may occur.

4.1. Warm Shear Regime (WSR)

The primary indicator for this flow regime is the MTI stopping signature, a backward propagating shock (Figure 4b). This occurs for snow temperatures slightly below 0, and liquid water content may play a role (Figure 5). For these snow characteristics, it was shown by Steinkogler, Gaume et al., (2015) that aggregation exceeds fragmentation and should give rise to the formation of persistent-moist granules. These granules can have a diameter of several decimeters (Bartelt & McArdell, 2009). The deposition due to piling up of material and the relatively high velocities reached by these flows, up to $\approx$ 25 m/s, suggest that the cohesive forces acting between granules are not sufficient to glue particles together into larger units. They may flow as a viscoplastic material with kinetic stresses above the yield strength, and shearing is possible. The MTI flowing signature is homogeneous (Figure 3a), further suggesting that the flow is fluid-like rather than solid-like; that is, it is sheared throughout its depth so that the surface is steadily changing. We define this flow regime as *warm shear regime* (WSR).

4.2. Warm Plug Regime (WPR)

This flow regime occurs when the snow cover temperature is isothermal, $T = 0°C$, with a median liquid water content of 1.8% (Figure 5). These snow cover characteristics are an indication of the formation of large persistent-wet granules (Steinkogler, Gaume et al., 2015). The MTI flowing signature reveals parallel streaks (Figure 3e), probably corresponding to large granules or surface undulations which are transported at the avalanche surface over large distances, indicating very little mixing during the flow; that is, the surface is a pseudoplug. Blank spots in the MTI images may belong to parts of the flow where the surface is smooth. The velocity is typically less than 10 m/s (Figure 5). Since the velocities are relatively low and cohesion between granules is large, they can easily stick together and give rise to large flow units which behave like gliding,

solid-like blocks (Issler, 2003). These are most likely flowing as a viscoplastic fluid with a large pseudoplug region and usually stop abruptly (Figure 4c). The MTI data suggest that these blocks can be up to 100 m long (Figure 8d). Deposit investigations and pictures confirm these large flow units and highlight the presence of a former granular structure, shear planes, gliding surfaces, and levees (Figure 1c). We define this flow regime as *warm plug regime* (WPR).

4.3. Intermittent Regime (IR)

In the frontal region of a fully developed PSA, the MTI flowing signature is characterized by short streaks lasting a few seconds, which indicate an intense surging activity (Figure 3c). These minor surges can flow up to 50 % faster than the avalanche front. Once the internal surges reach the front they quickly decelerate and starve giving the front an intermittent character (Köhler et al., 2016). The typical MTI stopping signature of these regions is characterized by multiple surges at the front and starving at the tail (Figure 4a). For this regime, snow temperature is always below −2°C; thus, granulation does not occur or is rather limited, and fragmentation of released and entrained snow cover gives rise to fine grained material. Further characteristics of this flow regime are flow heights up to 9 m with velocities as high as 60 m/s (blue cluster in Figure 6). We define this flow regime as *intermittent regime* (IR), and it was described in detail in Sovilla et al. (2015).

4.4. Cold Dense Regime (CDR)

Not all cold avalanches develop an IR. These cold avalanches do not exceed a flow height of 4 m and have a velocity below 30 m/s (Figure 6). Similar to those with the IR, they are characterized by the starving stopping mechanism. We expect that given the right topography, for example, a concave path or a strong increase in roughness, these flows may also stop with a backward propagating shock (Gray et al., 2003). These flows are often concentrated in a single surge. Such a single surge gives a homogeneous MTI flowing signature and does not exhibit internal line features (Figure 3b). We speculate that these avalanches consist of grains in solid contact behaving like a dry granular flow with negligible influence from the air. We define this flow regime as *CDR*.

In several CDR flows, MTI plots show triangular shaped features at specific ranges (Figure 3h). We interpret these features as standing waves or shocks (Gray et al., 2003; Faug et al., 2015) or even jets (Hákonardóttir et al., 2003), perhaps initiated by obstructions and terrain features such as changing roughness, slope (Hopfinger, 1983), or narrowing width of the couloir. Standing shocks occur when the flow is supercritical; that is, the Froude number is greater than 1, so that their existence is dependent on flow height and velocity. In avalanche both parameters are normally highest at the front and subsequently decrease toward the tail. This could explain the triangle shape: for a fast front with large flow heights, the shock may extend a long way forward from the obstruction. And as soon as both parameters decrease, the shock moves upward and closer to the obstruction (Figure 9a). For a jet, the downslope distance varies with the flow velocity and the launching angle, and again both parameters change over time. The launching angle depends on the inclination of the obstruction's upstream face and may change due to smoothing by the flow itself (self-ramping). If the Froude number is high enough, other instabilities such as roll waves (Figure 1b) may develop and there is some evidence for this (Köhler et al., 2016).

4.5. Snowball Regime (SBR)

Avalanches containing warm snow can give rise to individual snowballs or snow wheels rolling down the slope (Figure 3e). They show up as individual lines with speeds of up to 20 m/s. The snowballs usually come out of WPR or WSR regions, indicating their granular composition, but fragments in cold avalanches can also show similar behavior (Figure 1b). We call this regime *snowball regime* (SBR).

4.6. Sliding Slab Regime (SSR)

Most cold avalanches and occasionally warm avalanches start with a slab failure. This gives an MTI starting signature of a vertical line. The lowest point of this line can be tracked to follow the initial acceleration of the slab (Figure 3j). The slab fractures almost instantaneously after release, and each individual fragment starts to slide downslope (Figure 1e). The fracturing process can last for up to 200 m until the avalanche consists of small snow clods (Issler, 2003) and transitions into a dense regime. We call this regime the *sliding slab regime* (SSR).

4.7. Suspension Regime (SR)

The GEODAR does not measure the avalanche powder cloud since the cloud consists of single snow grains at the millimeter scale. However, this flow regime can be observed with videogrammetry or photogrammetry

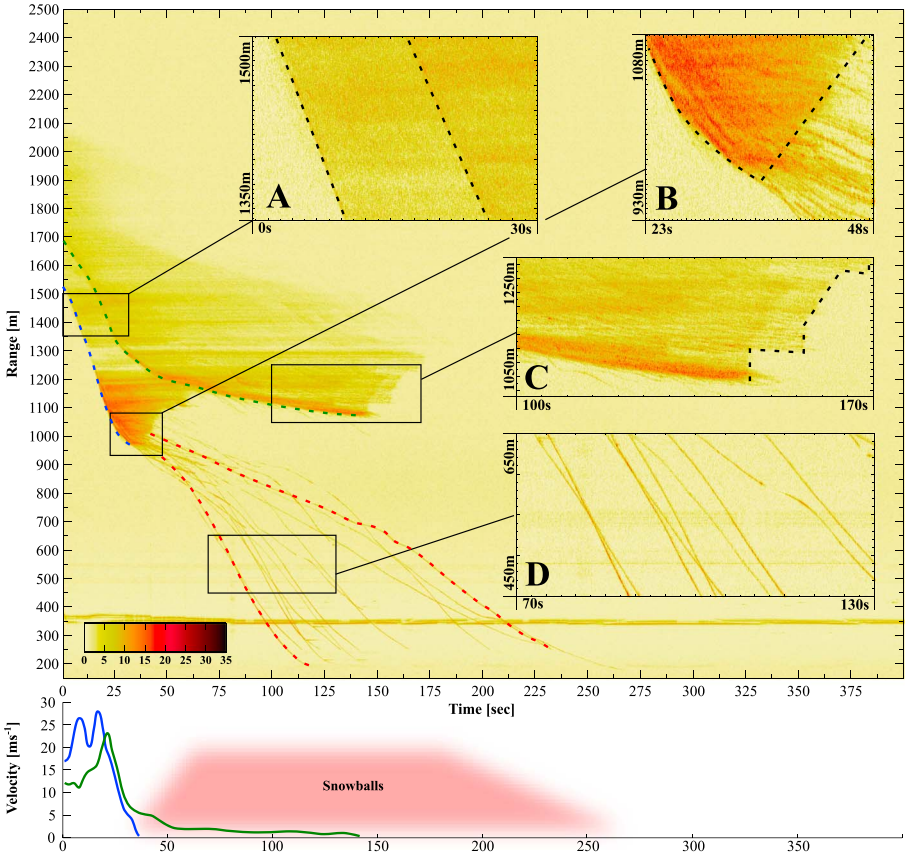

Figure 7. Avalanche #12-3060 naturally released on 15 March 2012 from Pra Roua. This avalanche is mostly representative of the warm shear regime. The avalanche release was not recorded, and GEODAR first captured the avalanche when two laterally displaced fronts entered the couloir. While most of the avalanche stopped at the end of the couloir, snowballs continued to roll for up to 1 km (snowball regime).

(Turnbull & McElwaine, 2007) and detected with air pressure and density sensors and is listed here for completeness. The powder cloud height is much larger than the denser parts of the flow, and it accompanies the IR or sometimes an avalanche exhibiting only a CDR. While the denser parts disappear in shadow areas in the avalanche path (Figure 2), a suspension cloud can extend well above (Figure 1a). Since there is still some MTI intensity (Figure 3f) , the suspension regime may transport a few larger snow clods. We call this regime the *suspension regime* (SR).

5. Avalanche Examples

Avalanches at the Vallée de la Sionne are always characterized by a combination of two or more flow regimes. In order to show the most relevant flow regimes and combinations of them, we present four different avalanche examples extracted from our database. The first two examples contain mainly warm snow, whereas the later two examples contain cold or mostly cold snow.

5.1. Avalanche #12-3060: Mainly Warm Shear

Avalanche #12-3060 naturally released in the morning of 15 March 2012 (Figure 7). Although the avalanche release was not captured by the GEODAR, pictures show that the avalanche started as a full-depth avalanche and eroded some soil (Figure 1d). The average snow cover temperature to 50 cm depth at the upper weather station was −1.9°C, but we expect that the avalanche started already with warm snow because typical freezing cycles in spring conditions bias the temperature estimation (section 2.4).

The avalanche had developed the typical characteristics of a *WSR* with an homogeneous colored MTI plot (Figure 7a), and no internal structures such as internal streaks close to the front as indicative of surges or roll waves.

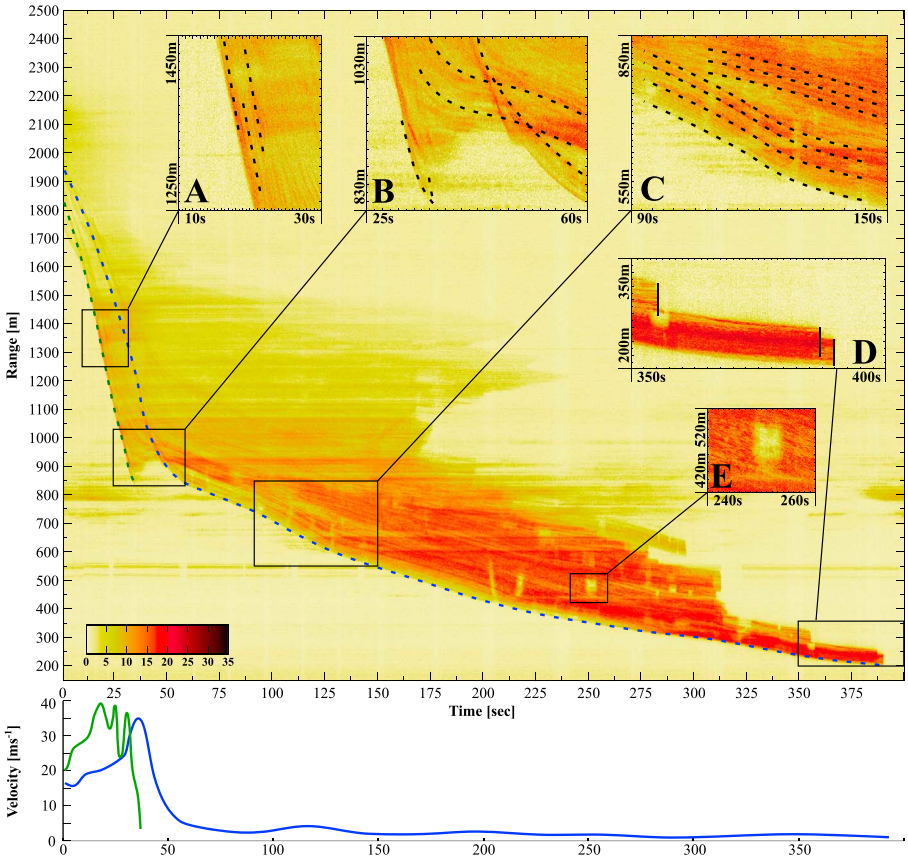

Figure 8. Avalanche #13-3019 naturally released on 1 of February 2013 from Crêta Besse 1/2. This avalanche is a typical example of transitional flow characterized by cold regimes in the upper part of the flow and a transition to the warm plug regime starting from 900 m range. This range approximately corresponds to the snowfall limit, below which the rain wetted the snow cover. The first front starves at the end of the couloir, but the second front turns into the warm plug regime and continues until the valley floor.

The example consisted of two fronts which entered the couloir at different locations (Figure 7a). The first front entered the couloir with a velocity of around 20 to 25 m/s before deceleration started at 1,150 m, bringing the first front to rest at 950 m. The second front was captured from 1,700 m range onward. Its velocity increased from 12 m/s to slightly over 20 m/s in the couloir. As it hit the deposits of the first front at 1,200 to 1,300 m, it decelerated to only 2 m/s and stopped at 1,080 m. The front velocity of avalanches in the WSR is in general medium fast and react to changes in the terrain and flow path.

The SBR shows up as lines starting from the deposit of the first front (Figure 7b) and continued until the valley floor (Figure 7d). The second front showed these granules as well, but they did not travel as far (Figure 7c). Probably they were stopped on the rough surface of the deposit from the first front. These snowballs come from already existing large granules formed earlier and show the granular composition of the WSR (Figure 1d).

The main stopping mechanism characterizing this avalanche (Figure 7b) is the backward propagating shock (Figure 4b). However, especially in the deposit of the second surge (Figure 7c), the characteristics of the abrupt stopping mechanism (Figure 4c) can be also recognized. This suggests that the second front may already have partially evolved into a WPR.

5.2. Avalanche #13-3019: From Cold to Warm Plug

Avalanche #13-3019 naturally released on 1 February 2013 during a snow storm with a rain limit at 2,000 m a.s.l (Figure 8). Although the avalanche release was not captured by the GEODAR, we expect that the avalanche started as a cold slab since the average snow cover temperature at the top weather station, in the upper 50 cm of snow cover, was −2.2°C.

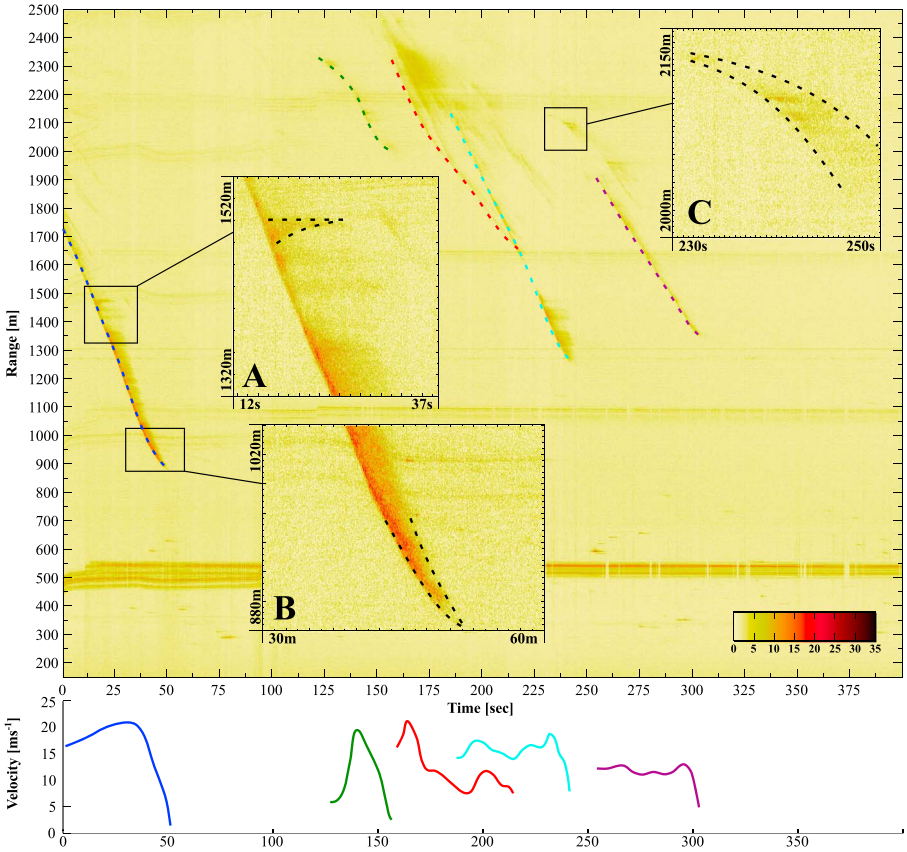

Figure 9. Multiple small avalanches occurred on 6 December 2012 between Crêta Besse 1 and 2 (#13-3005). These avalanches are typical examples of the cold dense regime. They have a remarkably short flowing length of only around 100 m, and they are characterized by a single surge.

The GEODAR was switched on when the avalanche reached the range 1,800 to 2,300 m. The first front entered the couloir with a velocity of up to 40 m/s and stopped at around 850 m with the starving nose mechanism (Figure 4a). A small IR can also be identified by the characteristic streak signature (Figure 8a).

The WPR started at 900 m (Figure 8b) and continued until the valley floor. The average front velocity of the WPR region was only 2 to 3 m/s. The WPR can be recognized by the existence of several semi-independent flow units. Each of these viscoplastic units moved with almost uniform velocity. The picture in Figure 1c suggest that single packages are separated by levees with steep and icy shear planes (Issler, 2003). Since each unit is sliding as a solid-like block, any surface unevenness moves coherently and gives rise to the characteristic MTI flowing signature of parallel streaks (Figure 8c) or even blank spots in the MTI (Figure 8e). All these flow units stopped with the abrupt stopping mechanism (Figure 8d).

It is possible to recognize a region with a backward propagating stopping shock (Figure 4b) in the avalanche tail at a range of around 1,200 m and time of 200 s, indicating that the avalanche tail may here developed a WSR. This range corresponds to an altitude below the rain limit (Figure 2) and also to the end of the steep couloir.

5.3. Avalanche #13-3005: Mainly Cold Dense

The avalanches in Figure 9 are examples of the CDR, as the average snow temperature in the release area was −9.8°C. These small avalanches released as small slabs or as point releases (Figure 9c) and typically started depositing at the end of the couloir. These example avalanches had a flowing length of only around 100 m. Other avalanches in the CDR can have a larger length, but it is remarkable that avalanches with such a short flowing length can maintain their movement over distances as long as 1,500 m.

These CDR avalanches have a homogeneous MTI flowing signature with no internal features like streaks, and they are normally characterized by a single surge. A single triangular feature exists at a range of 1,480 m

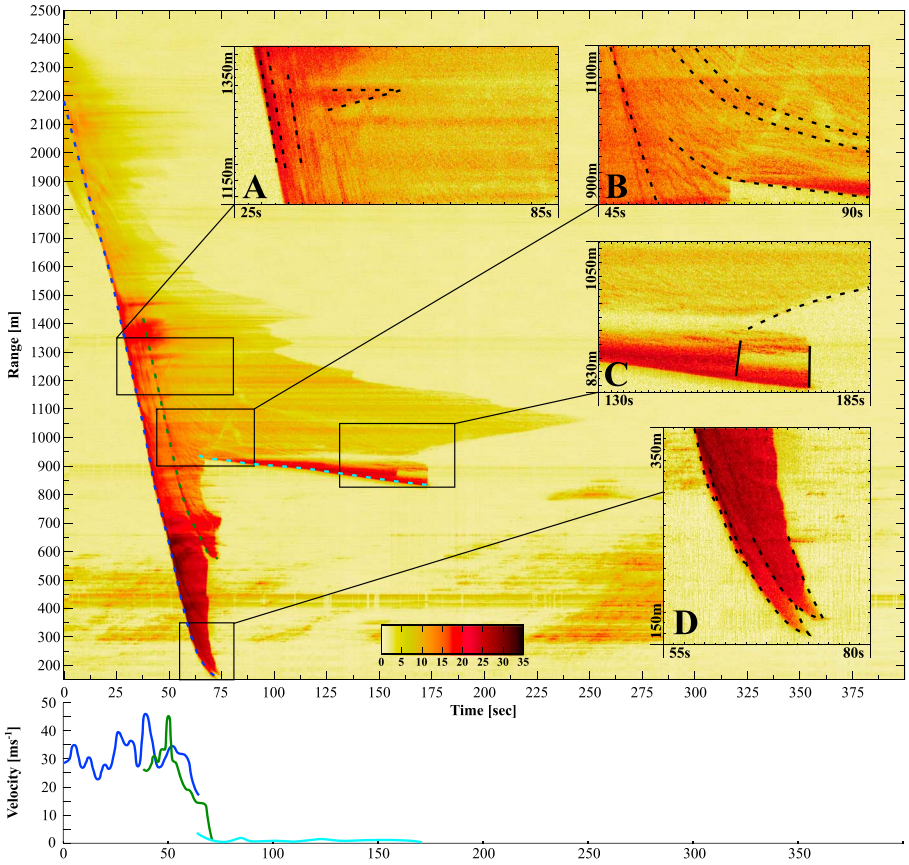

Figure 10. A fully developed powder snow avalanche #14-0012 occurred on 13 February 2014 from Crêta Besse 1. The avalanche is characterized by up to six different flow regimes, indicating a complex interplay between cold and warm snow.

(Figure 9a). The signal strength gradually decreases toward the tail (Figure 9b). This is in agreement with the FMCW radar data from Cavern B which showed a smooth and continuous decrease in flow height between front and tail, while the maximum flow depth did not exceed 3 to 4 m (Figure 6).

The avalanches quickly reached a steady state velocity, where gravity was in approximate balance with the effective basal friction. Usually, the front velocity is in the range of 10 to 20 m/s. As the examples in Figure 9 show, the velocity was relatively constant over a large portion of the avalanche trajectories. The front velocity was surprisingly insensitive to the slope of the terrain as there is no further acceleration at the entrance of the couloir. At one point, the avalanches started to decelerate, and stopped with the starving stopping signature (Figure 9b).

5.4. Avalanche #14-0012: Fully Developed PSA

The front of a PSA, such as in Figure 10, appears as a straight line in the GEODAR data from shortly after the initiation to shortly before deposition. Thus, the front velocity seems to be fairly independent of terrain. Note however that this front is not in general the front of the powder cloud since fine snow grains are not imaged by the radar. Instead, the signal comes from large blocks in the intermittent region or the dense core. In the example avalanche in Figure 10 the front velocity was around 35 m/s with a slight acceleration as it entered the steep couloir. It is this location where the MTI flowing signature becomes darker and streaks indicate the beginning of the IR (Figure 10a). Köhler et al. (2016) defined these streaks as minor surges of the IR, which can flow with higher velocity than the front, and by overtaking it caused shooting-like movement and a discontinuous front velocity. After the passage of the IR, the MTI flowing signature becomes more homogeneous (Figure 10a) indicating the evolution of the flow toward a CDR.

The MTI stopping signature at the final runout (Figure 10d) indicates starving (Figure 4a). Köhler et al. (2016) suggested that a starving starts as soon as all minor surges from the IR have overtaken the front. Indeed,

the GEODAR data in Figure 4a supports this hypothesis by showing the starving of many minor surges before finally the nose stops.

Finally, a slow moving flow feature evolved at the end of the couloir (Figure 10b), showing the typical MTI flowing signatures of the WPR (Figure 10c). This feature moved with velocities of only 1 to 2 m/s and came to rest with the abrupt MTI stopping signature (Figure 4b). Some parts of this feature also exhibited a backward propagating shock (Figure 4c).

6. Flow Regime Transitions

As shown in the previous examples, a single avalanche can be characterized by multiple flow regimes. The understanding of the physical processes governing flow regime transitions is thus of fundamental importance to predict the avalanche dynamics. Particularly relevant are transitions between the main five flow regimes, namely suspension, cold dense, intermittent, warm shear, and WPR.

The first important transition can be observed in cold avalanches that normally starts as dense flows. Small avalanches often stay in this CDR, but medium to large flows usually develop an IR (Figure 6) and a SR. The flow transition between CDR and IR typically occurs at the entrance of the couloir below 1,500 m and manifests itself with the typical streak MTI flowing signature and darker spots in the MTI plots (Figure 10). As previously discussed, the darker MTI flowing signature could be the result of rougher terrain causing increased agitation in the flow, perhaps a higher granular temperature or higher turbulent energy. The lines result from internal surges near the avalanche front (Köhler et al., 2016). The origin of the surges is not completely clear yet, but since they occur as soon as the avalanche reaches a certain size and speed, this suggests that they are a flow instability such as roll waves. Figure 6 suggests that surges build above a velocity of 20 to 30 m/s. This is in accordance with the findings of Gauer et al. (2008) that the effective friction, in their words the retarding acceleration, changes at similar velocities. The surges have a life time of a few seconds, and the longitudinal extent of the IR is usually up to a couple of hundred meters.

The second relevant flow transition observable in our data set occurs in warm avalanches and manifests itself as a change from a shear regime to a plug flow regime (strictly speaking this is a pseudoplug, that is, a region which is at the yield stress so that it has solid-like behavior but still deforms). Typically, the plug flow regime starts in the shallow deposition region below the couloir. When the slope is gentle so that the flow is slower and experiences less agitation from the base, and the flow depth and thus the overburden pressure are large, the full avalanche can transform into the WPR (Figure 8). Such a transition can occur also locally (Figure 3i) or partially (Figure 7c). This process may be explained by the granular nature of the flow and specifically by the balance between forces which promote aggregation and forces which induce fragmentation (Issler, 2003; Steinkogler, Gaume et al., 2015). In particular, the yield strength increases with particle cohesion and overburden pressure, whereas fragmentation forces such as shear and impact stresses increase with velocity and slope angle. To which extent a viscoplastic flow (a pure plug over a sheared layer, Kern et al., 2004), a cohesive granular flow, or a polydisperse flow (thick sheared layer above a highly sheared layer, Rognon et al., 2008, 2007) is more appropriate to represent such a transition is an actual debate (Ancey, 2007). Additionally, one may consider segregation of faster and slower material, or colder and warmer material, inside the avalanche and mixing with warmer snow cover due to entrainment as a possible cause for the transition between WSR and WPR.

Finally, another important flow transition occurs when a cold avalanche transforms into a warm avalanche. Even though most of the snow flowing inside a PSA is cold, entrainment of deeper and warmer layers can raise the temperature to that of warm snow, with the result that the passage between warm and cold flow happens toward the avalanche tail and manifests itself with the formation of a creeping tail (Figure 10). If, however, the full snow cover is warm, the flow regime transition can occur directly at the front and control the complete flow dynamics. Indeed, the avalanche in Figure 8 shows the typical features of a large PSA which transforms completely into a plug flow below 1,000 m range. It is remarkable, that this transition occurs in only a few seconds and within a distance of around 100 m and is most likely the result of rain precipitation warming and wetting the snow cover at lower altitudes. Nearly all the potential energy in an avalanche will heat up the flowing snow due to friction. Steinkogler, Sovilla, and Lehning (2015) found a temperature increase of 0.3°C per 100 m drop height, but entrainment of snow at lower altitudes and from deeper layers in the

snow cover can be a much more effective mechanism to change the snow temperature inside the avalanche (Steinkogler et al., 2014), since entrainment can increase the total flowing mass by an order of magnitude (Sovilla et al., 2006).

7. Conclusions

The GEODAR system has collected data on 77 avalanche events since 2009/2010. The avalanches show a wide variety of different dynamic behavior and flow regimes. We have analyzed the MTI flowing signatures such as lines and streaks or darker and light colored spots and conclude that streaks are the signature of internally moving features and characteristic spots originate from the interaction of the avalanche with the terrain causing features such as standing waves. Further, the MTI plots show that there are three dominant stopping mechanisms, primarily determined by the snow temperature and liquid water content. These snow cover parameters mainly control the cohesion and cause the flowing snow to aggregate into granules or even clump together into large flow units. Cold snow tends to stop from the tail with a decrease in length of the flowing region behind the head, whereas warm snow tends to stop first at the front followed by a progressive pileup, and a large plug flow unit can stop instantaneously.

Seven flow regimes have been defined on the basis of the GEODAR data. This list of flow regimes provides an exhaustive classification of the avalanches observed at Vallée de la Sionne. The GEODAR data can show the evolution of these flow regimes in time and space and characterize transitions between them. While small to medium sized avalanches tend to be *simple* with only one flow regime, larger avalanches are *complex* and exhibit multiple flow regimes simultaneously. One reason for this is that large avalanches tend to cover a great range of altitudes (> 1,000 m) and therefore experience a greater range of snow conditions.

Two of the seven flow regimes, the sliding slab and the SBR, are only of marginal interest in the big picture of an avalanche. But the sliding and break up of slabs become important in respect to the entrainment process due to secondary releases (Köhler et al., 2016). And the rolling of snowballs can be seen as the "contactless" granular limit of the WSR. Rolling granules can not only reach farther runouts but may even trigger secondary avalanches.

The other five flow regimes should be included in physically based numerical models. For many purposes, for example, hazard-zoning where good statistics are available, a physically based avalanche model is not always necessary. However, for scientific purposes where we wish to have models that correctly describe the underlying physics without containing empirically chosen fitting parameters, each of these regimes and transitions between them must be correctly modeled. Some of these regimes may be described by a single rheological model. For example, it may be possible to describe all the dense regimes CDR, WSR, and WPR by a model including plasticity (Ancey, 2007) parameterized by temperature and granule size.

The IR is an important part of our classification system that may be helpful in explaining the longevity and mobility of PSAs (Köhler et al., 2016), by significantly increasing the mass flux into the powder cloud and increasing the turbulent kinetic energy. New modeling concepts must be developed, since velocity and density variations (Sovilla et al., 2015) may not be described with standard depth-averaged numerical approaches, though there can be good agreement (Louge, 2014). Future work can build up on the descriptive terminology developed here and connect rheological properties of snow to the expression of flow regimes by combining our results with the wide field of cohesive and noncohesive granular flows.

Our observations of flow regimes in snow avalanches with the use of radar technology may also be important for other gravitational mass movements. For example, pyroclastic density currents may develop a similar flow regime as the IR of PSAs, but obtaining direct measurements in the hot ash is significantly harder. The advantage of using snow avalanches as an example flow process is the frequent return period and the possibility to control the release artificially.

To aid in the development of numerical models all of the data in this paper are released under a creative commons license. For users of this data, this paper also functions as a useful aid to understand the MTI plots and their features.

We also hope that this data set will attract the interest of those in the image-processing and machine-learning communities. If automatic algorithms for processing the GEODAR data can be developed, the radar data can be unambiguously and objectively interpreted without additional local point measurements. We hope that

this work will spur the deployment of similar radar systems to study other mass flows and both improve scientific understanding and have practical benefits for warning systems and road and infrastructure security.

Appendix A: List of Acronyms

VdlS	Vallée de la Sionne
PRA	Release area around summit "Pra Roua"
CB	Release area ridge "Crêta Besse" with numbers 1 and 1/2, and summit with 2
GEODAR	GEOphysical flow dynamics using pulsed Doppler radAR
FMCW	Frequency-modulated continuous wave
MTI	Moving target identification, for example, used in GEODAR images
VDS2	Weather station "Donin du jour" at 2,390 m a.s.l., subscript $_t$
VDS3	Weather station close to the pylon at 1,680 m a.s.l., subscript $_b$
WPR	Warm plug regime
CDR	Cold dense regime
WSR	Warm shear regime
IR	Intermittent regime
SBR	Snowball regime
SSR	Sliding slab regime
SR	Suspension regime
PSA	Powder snow avalanche

Appendix B: GEODAR Data Repository

All the GEODAR data discussed in this paper and listed in Table 1 are open access and stored in the Zenodo (https://zenodo.org/) data repository, which is financed by the Horizon 2020 project OpenAIRE and hosted by CERN. The associated entry can be accessed via the following:

> McElwaine*, J. N., A. Köhler*, B. Sovilla, M. Ash, and P. V. Brennan (2017), GEODAR data of snow avalanches at Vallée de la Sionne: Seasons 2010/2011, 2011/2012, 2012/2013 & 2014/2015 [Data set]. *Zenodo*. doi:10.5281/zenodo.1042108 . *equally contributing authors

The archive contains processed GEODAR data, namely, the MTI plots, plus some derived data such as the 1-D thalweg, the projected trajectory $s(t)$, and the downslope velocity $\dot{s}(t)$ of the front or surge. A document serves as metadata and contains details related to GEODAR. We give a comprehensive description of the different GEODAR versions, more technical details to the applied processing steps, the MTI filtering, the HDF5 data format, and how to access the data in the container. Finally, the bibliography list of all GEODAR-related publications serves as references.

Even though the data are generally open access, we highly recommend to contact the authors prior to usage. Even though we gained a substantial knowledge about the signal interpretation, the data are still not straightforward to use. We believe that only a culture of open discussion and collaboration can make the most out of this invaluable data set.

Supporting information as the meteo data and snowpack simulations used in this paper are not part of the data repository but are made available upon request.

Acknowledgments
The research was funded by the Swiss National Science Foundation (SNSF) project "High Resolution Radar Imaging of Snow Avalanches," grant 200021_143435; the test site and infrastructure by SNSF R'EQUIP project "Snow Avalanches in the Swiss experiment", grant 206021_113069/1; and the canton of Valais. Special thanks are due to our colleagues at the electronics and workshop of SLF for their invaluable support. We thank Barbara Turnbull, Thierry Faug, Alexander Densmore, and one anonymous referee for a careful reading of the manuscript and many helpful comments.

References

Ammann, W. J. (1999). A new swiss test-site for avalanche experiments in the Vallée de la Sionne/Valais. *Cold Regions Science and Technology*, *30*(1), 3–11. https://doi.org/10.1016/S0165-232X(99)00010-5

Ancey, C. (2007). Plasticity and geophysical flows: A review. *Journal of Non-Newtonian Fluid Mechanics*, *142*(1–3), 4–35. https://doi.org/10.1016/j.jnnfm.2006.05.005

Ash, M., Brennan, P. V., Chetty, K., McElwaine, J. N., & Keylock, C. J. (2010). FMCW radar imaging of avalanche-like snow movements. In *Proceedings of the 2010 IEEE Radar Conference* (pp. 102–107). Arlington, VA: IEEE. https://doi.org/10.1109/RADAR.2010.5494643

Ash, M., Tanha, M. A., Brennan, P. V., Köhler, A., McElwaine, J. N., & Keylock, C. J. (2015). Practical implementation of a 16-channel C-band phased array radar receiver. In *Proceedings of the 2015 IEEE Radar Conference* (pp. 66–70). Sandton, South Africa: IEEE. https://doi.org/10.1109/RadarConf.2015.7411856

Bartelt, P., & McArdell, B. W. (2009). Instruments and methods: Granulometric investigations of snow avalanches. *Journal of Glaciology*, *55*(193), 829–833. https://doi.org/10.3189/002214309790152384

Brennan, P. V., Ash, M., Isa, F. M., Keylock, C. J., & McElwaine, J. N. (2009). Advanced radar imaging of geophysical flows. In L. Trilling, et al. (Eds.), *3rd IASME/WSEAS International Conference on Geology and Seismology, Cambridge, Feb. 24-26, 2009* (pp. 144–147). Cambridge: WSEAS Press.

De Quervain, M. R., De Crecy, L., LaChapelle, E. R., Losev, K., & Shoda, M. (1973). Avalanche classification. *Hydrological Sciences Bulletin*, *18*(4), 391–402. https://doi.org/10.1080/02626667309494054

Faug, T., Childs, P., Wyburn, E., & Einav, I. (2015). Standing jumps in shallow granular flows down smooth inclines. *Physics of Fluids*, *27*(7), 73304. https://doi.org/10.1063/1.4927447

Gauer, P., Issler, D., Lied, K., Kristensen, K., & Sandersen, F. (2008). On snow avalanche flow regimes: Inferences from observations and measurements. In *International Snow Science Workshop* (pp. 717–723). Whistler, Canada.

Gray, J. M. N. T., Tai, Y.-C., & Noelle, S. (2003). Shock waves, dead zones and particle-free regions in rapid granular free-surface flows. *Journal of Fluid Mechanics*, *491*, 161–181. https://doi.org/10.1017/S0022112003005317

Gubler, H., & Hiller, M. (1984). The use of microwave FMCW radar in snow and avalanche research. *Cold Regions Science and Technology*, *9*(2), 109–119. https://doi.org/10.1016/0165-232X(84)90003-X

Hákonardóttir, K. M., Hogg, A. J., Batey, J., & Woods, A. W. (2003). Flying avalanches. *Geophysical Research Letters*, *30*(23), 2191. https://doi.org/10.1029/2003GL018172

Hopfinger, E. J. (1983). Snow avalanches motion and related phenomena. *Annual Review of Fluid Mechanics*, *15*, 47–96. https://doi.org/10.1146/annurev.fl.15.010183.000403

Issler, D. (1998). Modelling of snow entrainment and deposition in powder-snow avalanches. *Annals of Glaciology*, *26*(1), 253–258. https://doi.org/10.1017/S0260305500014919

Issler, D. (2003). Experimental information on the dynamics of dry-snow avalanches. In K. Hutter, & N. Kirchner (Eds.), *Dynamic response of granular and porous materials under large and catastrophic deformations* (Vol. 11, pp. 109–160). Berlin: Springer. https://doi.org/10.1007/978-3-540-36565-5_4

Kern, M. A., Tiefenbacher, F., & McElwaine, J. N. (2004). The rheology of snow in large chute flows. *Cold Regions Science and Technology*, *39*(2–3), 181–192. https://doi.org/10.1016/j.coldregions.2004.03.006

Keylock, C. J., Ash, M., Vriend, N., Brennan, P. V., McEwaine, J. N., & Sovilla, B. (2014). Looking inside an avalanche using a novel radar system. *Geology Today*, *30*(1), 21–25. https://doi.org/10.1111/gto.12033

Köhler, A., McElwaine, J. N., Sovilla, B., Ash, M., & Brennan, P. V. (2016). The dynamics of surges in the 3 February 2015 avalanches in Vallée de la Sionne. *Journal of Geophysical Research: Earth Surface*, *121*, 2192–2210. https://doi.org/10.1002/2016JF003887

Lehning, M., Bartelt, P., Brown, B., & Fierz, C. (2002). A physical SNOWPACK model for the Swiss avalanche warning part III: Meteorological forcing, thin layer formation and evaluation. *Cold Regions Science and Technology*, *35*(3), 169–184. https://doi.org/10.1016/S0165-232X(02)00072-1

Louge, M. Y. (2014). The surprising relevance of a continuum description to granular clusters. *Journal of Fluid Mechanics*, *742*, 1–4. https://doi.org/10.1017/jfm.2013.650

Naaim, M., Durand, Y., Eckert, N., & Chambon, G. (2013). Dense avalanche friction coefficients: Influence of physical properties of snow. *Journal of Glaciology*, *59*(216), 771–782. https://doi.org/10.3189/2013JoG12J205

Pérez-Guillén, C., Sovilla, B., Suriñach, E., Tapia, M., & Köhler, A. (2015). Deducing avalanche size and flow regimes from seismic measurements. *Cold Regions Science and Technology*, *121*, 25–41. https://doi.org/10.1016/j.coldregions.2015.10.004

Rognon, P. G., Roux, J.-N., Naaim, M., & Chevoir, F. (2007). Dense flows of bidisperse assemblies of disks down an inclined plane. *Physics of Fluids*, *19*(5), 58101. https://doi.org/10.1063/1.2722242

Rognon, P. G., Roux, J.-N., Naaim, M., & Chevoir, F. (2008). Dense flows of cohesive granular materials. *Journal of Fluid Mechanics*, *596*, 21–47. https://doi.org/10.1017/S0022112007009329

Salm, B., & Gubler, H. (1985). Measurement and analysis of the motion of dense flow avalanches. *Annals of Glaciology*, *6*, 26–34. https://doi.org/10.1017/S0260305500009939

Schaerer, P. A., & Salway, A. A. (1980). Seismic and impact-pressure monitoring of flowing avalanches. *Journal of Glaciology*, *26*(94), 179–187. https://doi.org/10.1017/S0022143000010716

Schmid, L., Heilig, A., Mitterer, C., Schweizer, Jürg, Maurer, H., Okorn, R., & Eisen, O. (2014). Continuous snowpack monitoring using upward-looking ground-penetrating radar technology. *Journal of Glaciology*, *60*(221), 509–525. https://doi.org/10.3189/2014JoG13J084

Sovilla, B., Burlando, P., & Bartelt, P. (2006). Field experiments and numerical modeling of mass entrainment in snow avalanches. *Journal of Geophysical Research*, *111*, F03007. https://doi.org/10.1029/2005JF000391

Sovilla, B., McElwaine, J. N., Schaer, M., & Vallet, J. (2010). Variation of deposition depth with slope angle in snow avalanches: Measurements from Vallée de la Sionne. *Journal of Geophysical Research*, *115*, F02016. https://doi.org/10.1029/2009JF001390

Sovilla, B., McElwaine, J., Steinkogler, W., Hiller, M., Dufour, François, Suriñach, E., et al. (2013). The full-scale avalanche dynamics test site Vallée de la Sionne. In *International Snow Science Workshop* (pp. 1350–1357). France: Grenoble–Chamonix.

Sovilla, B., McElwaine, J. N., & Louge, M. Y. (2015). The structure of powder snow avalanches. *Comptes Rendus - Physique*, *16*(1), 97–104. https://doi.org/10.1016/j.crhy.2014.11.005

Steinkogler, W., Sovilla, B., & Lehning, M. (2014). Influence of snow cover properties on avalanche dynamics. *Cold Regions Science and Technology*, *97*, 121–131. https://doi.org/10.1016/j.coldregions.2013.10.002

Steinkogler, W., Sovilla, B., & Lehning, M. (2015). Thermal energy in dry snow avalanches. *Cryosphere*, *9*(5), 1819–1830. https://doi.org/10.5194/tc-9-1819-2015

Steinkogler, W., Gaume, J., Löwe, H., Sovilla, B., & Lehning, M. (2015). Granulation of snow: From tumbler experiments to discrete element simulations. *Journal of Geophysical Research: Earth Surface*, *120*, 1107–1126. https://doi.org/10.1002/2014JF003294

Swiss Geoportal (2015). *Federal Office of Topography, Wabern, Switzerland*, 2015. accessed: 30 September 2015.

Tanha, M. A., Brennan, P. V., Ash, M., Köhler, A., & McElwaine, J. N. (2017). Overlapped phased array antenna for avalanche radar. *IEEE Transactions on Antennas and Propagation*, *65*(8), 4017–4026. https://doi.org/10.1109/TAP.2017.2712183

Turnbull, B., & Bartelt, P. (2003). Mass and momentum balance model of a mixed flowing/powder snow avalanche. *Geophysical survey*, *24*(5–6), 465–477. https://doi.org/10.1023/B:GEOP.0000006077.82404.84

Turnbull, B., & McElwaine, J. N. (2007). A comparison of powder snow avalanches at Vallée de la Sionne with plume theories. *Journal of Glaciology*, *53*(180), 30–40. https://doi.org/10.3189/172756507781833938

UNESCO (1981). *Avalanche atlas: Illustrated international avalanche classification*, Natural Hazards, International Commission on Snow and Ice, UNESCO, Paris.

Voellmy, A. (1955). Über die Zerstörungskraft von Lawinen (On the destructive forces of avalanches). *Schweizerische Bauzeitung*, *73*(15), 212–217.

Vriend, N. M., McElwaine, J. N., Sovilla, B., Keylock, C. J., Ash, M., & Brennan, P. V. (2013). High-resolution radar measurements of snow avalanches. *Geophysical Research Letters, 40*, 727–731. https://doi.org/10.1002/grl.50134

Wever, N., Fierz, C., Mitterer, C., Hirashima, H., & Lehning, M. (2014). Solving Richards equation for snow improves snowpack meltwater runoff estimations in detailed multi-layer snowpack model. *Cryosphere*, *8*(1), 257–274. https://doi.org/10.5194/tc-8-257-2014